ANNUAL REVIEWS

The Evolution of the Star-Forming Interstellar Medium Across Cosmic Time

Linda J. Tacconi,[1] Reinhard Genzel,[1,2]
and Amiel Sternberg[3,4]

[1]Max-Planck-Institut für extraterrestrische Physik, 85748 Garching, Germany;
email: linda@mpe.mpg.de

[2]Departments of Physics and Astronomy, University of California, Berkeley, California 94720,
USA

[3]School of Physics and Astronomy, Tel Aviv University, Tel Aviv 69978, Israel

[4]Center for Computational Astrophysics, Flatiron Institute, New York, NY 10010, USA

ANNUAL REVIEWS CONNECT

www.annualreviews.org

- Download figures
- Navigate cited references
- Keyword search
- Explore related articles
- Share via email or social media

Keywords

galaxy formation, galaxy evolution, molecular gas, interstellar molecules,
star formation

Abstract

Over the past decade, increasingly robust estimates of the dense molecular
gas content in galaxy populations between redshift $z = 0$ and the peak of
cosmic galaxy/star formation ($z \sim 1$–3) have become available. This rapid
progress has been possible due to the advent of powerful ground- and space-
based telescopes for the combined study of several millimeter to far-IR, line
or continuum tracers of the molecular gas and dust components. The main
conclusions of this review are as follows:

- Star-forming galaxies contained much more molecular gas at earlier
  cosmic epochs than at the present time.
- The galaxy-integrated depletion timescale for converting the gas into
  stars depends primarily on z or Hubble time and, at a given z, on the
  vertical location of a galaxy along the star-formation rate versus stellar
  mass main sequence (MS) correlation.

- Global rates of galaxy gas accretion primarily control the evolution of the cold molecular gas content and star-formation rates of the dominant MS galaxy population, which in turn vary with cosmological expansion. Another key driver may be global disk fragmentation in high-z, gas-rich galaxies, which ties local free-fall timescales to galactic orbital times and leads to rapid radial matter transport and bulge growth. The low star-formation efficiency inside molecular clouds is plausibly set by supersonic streaming motions and internal turbulence, which in turn may be driven by conversion of gravitational energy at high z and/or by local feedback from massive stars at low z.
- A simple gas regulator model is remarkably successful in predicting the combined evolution of molecular gas fractions, star-formation rates, galactic winds, and gas-phase metallicities.

Contents

1. INTRODUCTION

It has been more than 40 years since the first detections of molecular gas in galaxies outside the Milky Way were published (Rickard et al. 1975, 1977; Solomon & de Zafra 1975; see also Young & Scoville 1991). Since then, it has become possible to map the distribution and kinematics of molecular gas in external galaxies with powerful (sub)millimeter interferometer arrays. The first high-redshift (high-z) CO detections in very luminous active galactic nuclei (AGN) and submillimeter galaxies (SMGs) were reported by Scoville et al. (1995, 1997) and Frayer et al. (1998, 1999), and the first detections of CO in normal high-z main sequence (MS) star-forming galaxies (SFGs) were presented by Tacconi et al. (2010) and Daddi et al. (2010a). Molecular gas[1] and dust studies of a few thousand normal SFGs from redshift $z = 0$ to $z = 4$ have been published in the last decade. The frontier is now at $z > 7$. Early concerns about the applicability of the CO-to-H_2 conversion factor have largely been allayed with the availability of dust-based estimates of molecular gas masses, at least on galaxy-integrated scales. While several recent reviews have summarized molecular gas studies (e.g., Carilli & Walter 2013, Combes 2018), in this article we strive to place studies of cold dense gas within the framework of cosmological galaxy formation and evolution. We begin by summarizing the properties of galaxy populations across cosmic time. We then show how knowledge of the cold gas content has provided critical new information on galaxy evolution. As we proceed, we emphasize the key physical processes and compare the observations with semianalytic models and hydrodynamic simulations (cf. Somerville & Davé 2015, Naab & Ostriker 2017). We conclude with questions that we believe are next on the agenda for substantial progress.

1.1. Star Formation in Molecular Clouds

Stars form from dusty, molecular interstellar gas (McKee & Ostriker 2007, Kennicutt & Evans 2012). In the Milky Way and nearby galaxies, all star formation appears to occur in massive ($M \sim 10^4 \ldots 10^{6.5} M_\odot$), dense [$n(H_2) \sim 10^2 \ldots 10^5$ cm^{-3}] and cold ($T_{gas} \sim 10$–40 K) (giant) molecular clouds [(G)MCs] of diameter $2R \sim 50$–100 pc (Solomon et al. 1987, Bolatto et al. 2008, McKee & Ostriker 2007). GMCs are highly supersonic [one-dimensional velocity dispersions, $\sigma \sim 0.7$ km s$^{-1} \times$ (R(parsec))$^{0.5}$] with Mach numbers of $\sim$30 (Larson 1981, Solomon et al. 1987, Elmegreen & Scalo 2004, Scalo & Elmegreen 2004). They are near but somewhat above virial equilibrium (i.e., unbound), with virial parameters $\alpha_V = 5\sigma^2 R/GM$ between 1 and 10 and a median of $\sim$2 (Miville-Deschenes et al. 2017, Meidt et al. 2018, Sun et al. 2018, Schruba et al. 2019). On scales of individual star-formation regions, clouds are likely transient, with GMC lifetimes of $t_{GMC} \sim$ 5–20 Myr due to disruption by protostellar outflows, ionized gas flows, and internal supernova explosions (e.g., Elmegreen 2007, Dobbs et al. 2011, Dobbs & Pringle 2013, Kruijssen et al. 2019, Chevance et al. 2020).

Star-formation rates (SFRs) on galactic scales, or star-formation surface densities on subgalactic scales down to a few kiloparsecs, are most strongly correlated with molecular gas (or dust) masses, or surface densities. There is little or no correlation between star formation and neutral atomic hydrogen at low surface densities (Kennicutt 1989; Wong & Blitz 2002; Kennicutt et al. 2007; Bigiel et al. 2008, 2011; Leroy et al. 2008, 2013; Schruba et al. 2011). It is not clear whether high molecular content is causally required for the onset of star formation (Glover & Clark 2012). More likely, high gas volume densities and sufficient dust shielding ($A_V > 7$; $\Sigma_{gas} > 100 M_\odot$ pc^{-2}) decouple the dense cores from the external radiation fields, allowing the clouds to cool rapidly and collapse. These conditions may then be naturally conducive to molecule formation, which

---

[1]Throughout this review, we correct H_2 masses upward by 1.36 for the content of helium and heavy elements for a census of the entire mass content of the molecular phase.

MS: the star-formation main sequence; a tight correlation between stellar mass and SFR for $\sim$90% of SFGs

SFGs: star-forming galaxies

Giant molecular cloud (GMC): has typical properties $M \sim 10^4 \ldots 10^{6.5} M_\odot$, $n(H_2) \sim 10^2 \ldots 10^5$ cm^{-3}, and $T_{gas} \sim$ 10–40 K

t_{GMC}: giant molecular cloud lifetime

SFR: star-formation rate (in $M_\odot$ year^{-1})

enhances further cooling (Sternberg & Dalgarno 1989, Heiderman et al. 2010, Krumholz et al. 2011, Glover & Clark 2012, Lada et al. 2012).

A self-gravitating molecular gas cloud of mean molecular hydrogen density ρ_{H_2} has a local free-fall time $t_{ff} = \sqrt{3\pi/(32G\rho_{H_2})}$. Heuristically, above a threshold of ~ 10 M$_\odot$ pc^{-2} (see Section 4.5), a self-gravitating cloud of total mass M should then form stars at a rate

$$\text{SFR} = \varepsilon_{ff} \times \frac{M}{t_{ff}}.$$

Here, ε_{ff} is the efficiency of star formation per free-fall time (cf. Kennicutt 1998, Elmegreen 2002, Krumholz & McKee 2005). For a homogeneous cloud supported by thermal gas motions, this efficiency (per free-fall time) should be high. For example, Alves et al. (2007), André et al. (2010), and Könyves et al. (2015) find a clump-to-star conversion efficiency of 20–40% in thermal cloud cores. However, since the first observations of molecular gas and cloud collapse in the Milky Way, it has become clear that on larger cloud and galactic scales the efficiency is small: $\varepsilon_{ff} \sim$ one to a few percent (Zuckerman & Evans 1974, Krumholz & Tan 2007).

There are two commonly accepted explanations for this low efficiency. One is that magnetic fields pervade the GMCs, which are frozen in because of trace ions created by cosmic-ray ionization. These fields stabilize the initially magnetically subcritical clouds against gravitational collapse (e.g., Mouschovias 1976, Shu et al. 1987). Ambipolar diffusion on a timescale of ~ 10 t_{ff} then allows a gradual collapse of the cloud. Observations suggest that cloud cores are magnetically supercritical and, thus, cannot be stabilized by magnetic pressure (Crutcher 2012). The second explanation rests on turbulent support. The highly supersonic gas motions in GMCs, and the interplay of dispersive and compressive shocks, prevent most of the gas from collapsing at any given time (Stone et al. 1998, Mac Low 1999, Klessen et al. 2000, Elmegreen & Scalo 2004, Krumholz & McKee 2005, McKee & Ostriker 2007). Since supersonic motions are dispersed on a dynamical time, the turbulent energy must be continuously replenished—within clouds, by outflows and supernova explosions, or by external gravitational torques or shear motions (Stone et al. 1998, McKee & Ostriker 2007).

1.2. Galaxy and Star Formation Across Cosmic Time

The formation/evolution of galaxies across cosmic time[2] is complex. It involves the hierarchical merging of virialized dark matter halos; the accretion and cooling of gas onto growing galaxies; and the formation of stars in cold dense gas clouds and outflows of heavy element–enriched gas into the circumgalactic medium (CGM), driven by massive stars, supernovae, and accreting supermassive black holes in the galaxy nuclei (e.g., Rees & Ostriker 1977; White & Rees 1978; White & Frenk 1991; Kauffmann et al. 1993; Croton et al. 2006; Bournaud & Elmegreen 2009; Dekel et al. 2009b; Dekel & Mandelker 2014; Bouché et al. 2010; Davé et al. 2011a,b, 2012; Guo et al. 2011; Lilly et al. 2013). Multiwavelength observations over the past 2 decades have provided an increasingly detailed picture of this baryonic cycle. Comprehensive studies show that the SFR density peaked approximately 3.5 Gyr after the Big Bang, at $z \approx 1.5$–2.5, and since then has declined by a factor of 10–15 to the present epoch, with an e-folding timescale of 4 Gyr (Lilly et al. 1996, Madau et al. 1996, Steidel et al. 1996, Madau & Dickinson 2014).[3] **Figure 1** depicts the cosmic star-formation

---

[2]Throughout this review, we use flat, ΛCDM (cold dark matter) cosmology with $H_0 = 70$ km s^{-1} Mpc^{-1} and $\Omega_m = 0.3$.

[3]Unless stated otherwise, we adopt a Chabrier (2003) or Kroupa (2001) initial stellar mass function, and have changed input values from the literature accordingly.
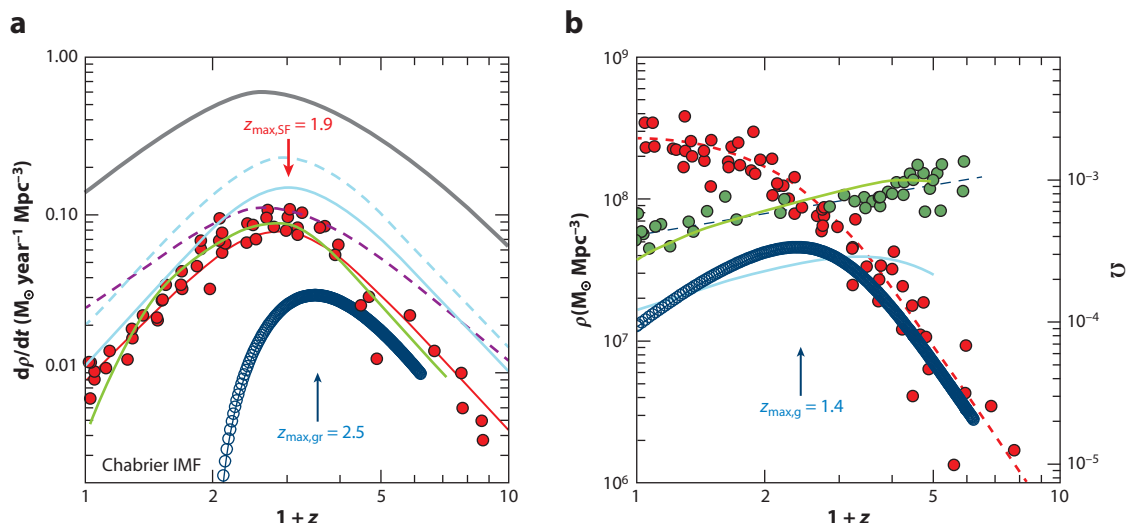
a

$z_{max,SF} = 1.9$

$z_{max,gr} = 2.5$

Chabrier IMF

$d\rho/dt$ ($M_\odot$ year^{-1} Mpc^{-3})

$1 + z$

b

ρ($M_\odot$ Mpc^{-3})

$z_{max,g} = 1.4$

$1 + z$

Figure 1

Cosmic evolutions of gas, stars, and massive black holes. (*a*) Evolution of cosmic star-formation history per comoving cosmic volume (*red filled circles*, *red fit function line*), from a wide range of UV to far-IR multiband surveys (Madau & Dickinson 2014, figure 9*c*). Shown for comparison are the rates of dark matter accretion (*thick gray line*), dark matter accretion divided by the cosmic dark matter/baryon ratio of 5.36 (*dashed purple line*), and the growth rate of massive black holes (*green line*) (Madau & Dickinson 2014, figure 15). The continuous and dashed light blue curves denote the baryon gas accretion rates required by the gas regulator model (Bouché et al. 2010, Lilly et al. 2013) for a wind mass loading factor of one and two, respectively. The thick blue-black curve is the rate of change of the molecular gas reservoir in galaxies estimated from this model. (*b*) Red circles denote the stellar mass in galaxies as observed in multiband estimates (Madau & Dickinson 2014, figure 11), and the dashed red line denotes the mass inferred from integrating the SFRs in panel *a*, for a Chabrier (2003) IMF and a return fraction R of 40%. The thick blue-black curve shows the evolution of the molecular mass (including helium) reservoir. Dark green filled circles and the connecting power-law fit (slope = 0.5) denote the evolution of atomic gas (Rhee et al. 2018). The light green and light blue curves denote the H I and molecular gas (H$_2$ × 1.36) content obtained in the MUFASA simulation of Davé et al. (2017). Panel *b* adapted with permission from Davé et al. (2017). Abbreviations: IMF, initial mass function; SFRs, star-formation rates.

history and stellar mass growth in galaxies inferred from the measurements (adopted from Madau & Dickinson 2014). The first galaxies condensed at $z \sim 8$–11, 350–550 Myr after the Big Bang (e.g., Bouwens et al. 2014, Oesch et al. 2016). Half the stellar mass observed today was formed prior to $z = 1.3$. Assuming a universal stellar initial mass function (IMF), the global stellar mass density at any epoch matches reasonably well with the time integral of all the preceding star-formation activity (**Figure 1*b***). The comoving rates of star formation and central black hole accretion follow a similar rise and fall, offering evidence for a sustained coevolution of black holes and their host galaxies (**Figure 1*a***) (Madau & Dickinson 2014). As we show in Sections 3 and 4, below, the comoving molecular gas densities and molecular gas fractions show a similar rise and fall, although these quantities are still very uncertain for $z > 3$.

1.3. The Star-Formation Main Sequence

Approximately 90% of cosmic star formation between $z = 0$ and $z = 2.5$ occurs in galaxies that lie along the so-called star-formation MS (Rodighiero et al. 2011, 2015). The MS is a fairly tight (±0.3 dex scatter), near-linear relationship between stellar mass and SFR (Brinchmann et al. 2004; Daddi et al. 2007; Elbaz et al. 2007, 2011; Noeske et al. 2007; Schiminovich et al. 2007; Peng et al. 2010; Rodighiero et al. 2010, 2011; Karim et al. 2011; Whitaker et al. 2012, 2014; Speagle et al. 2014; Renzini & Peng 2015; Schreiber et al. 2015).

For galaxies on the MS, the dependence of the specific SFR, sSFR = SFR/M_*, on stellar mass varies slowly with stellar mass as sSFR $\sim M_*^{-0.1–0.4}$, but the zero point increases very strongly with redshift: sSFR $\propto (1 + z)^3$ up to $z \sim 2$ and $\propto (1 + z)^{1.5}$ for $z > 2$ (e.g., Lilly et al. 2013). Several studies have captured these dependencies through empirical fittings to different galaxy samples from deep surveys (e.g., Whitaker et al. 2012, 2014; Speagle et al. 2014). The results are mostly in good agreement, with differences in zero points and slopes in the mass and redshift relations depending on sample selections (redshift range, survey bands), survey completeness, and methodologies applied to derive M_* and SFRs (Renzini & Peng 2015).

Except for passive galaxies at late times, or galaxies in dense environments, star-forming field galaxies mainly grew in mass along the MS through star formation (Guo & White 2008). The stellar mass function at all z has an exponential cutoff above the Schechter mass, $M_S \sim 10^{10.7–10.9}$ $M_\odot$ (Peng et al. 2010; Ilbert et al. 2010, 2013). Above this mass, star formation appears to quench (see the sidebar titled Quenching).

Figure 2 shows the MS lines derived by Speagle et al. (2014) and Whitaker et al. (2012, 2014), shown as log(sSFR) versus log(1 + z), corrected to a fiducial stellar mass of 5×10^{10} $M_\odot$, and as log(sSFR) versus log(M_*), corrected to a common redshift of $z = 1.5$. A crucial point is that the results differ dramatically depending on whether one infers SFRs from UV plus mid- or far-IR (24 µm or 70–160 µm) photometry or from spectral energy distribution (SED) fits; the UV+IR method generally accounts better for dust extinction and results in higher SFR estimates (e.g., Wuyts et al. 2011a). In practice, the UV+IR method is not available for all galaxies at $z > 3$ or for galaxies below the MS at $z > 1.5$. In this review, we adopt SFRs from the UV+IR methodology where possible, and from SED synthesis modeling for other cases—a strategy sometimes referred to as the ladder technique (Wuyts et al. 2011a).

> **Specific star-formation rate (sSFR):** SFR/M_*, where M_* is the stellar mass; sSFR normally has units of Gyr^{-1}

QUENCHING

The redshift-independent maximum stellar mass requires a strongly mass-dependent quenching process that terminates further mass growth and causes galaxies to transition from the star-forming MS population to the red sequence of passive galaxies (e.g., Kauffmann et al. 2004, Faber et al. 2007). It is not yet clear whether this quenching process originates at the scale of the dark matter halos, by transitions to hot, slow-cooling quasi-isothermal gaseous envelopes above halo masses $M_{crit} \sim 10^{12}$ $M_\odot$ (Rees & Ostriker 1977, Dekel & Birnboim 2006), or whether galaxy-internal processes are the main quenching drivers. For field galaxies, the probability of being quenched correlates most strongly with the central stellar surface density, Sersic index, and bulge mass (Kauffmann et al. 2003, Bell et al. 2012, Lang et al. 2014). This suggests that high-velocity outflows from the central black holes drive out gas from the galaxy and create hot, buoyant CGM atmospheres that prevent further accretion and quench star formation (Croton et al. 2006, Bower et al. 2017, Faerman et al. 2017, Nelson et al. 2019). Scaling relations of ionized outflows at $z \sim 1–2.5$ support this proposal (e.g., Genzel et al. 2014a, Harrison et al. 2014, Brusa et al. 2015, Förster Schreiber et al. 2019). In galaxy clusters and dense groups, starvation and harassment on large scales are additional mechanisms, even for lower-mass galaxies (Peng et al. 2010, 2015).

Blue SFGs on and above the MS, and red passive early-type galaxies below the MS, are well separated in UV/optical color–color space (Williams et al. 2009, Renzini & Peng 2015). SFRs are uncertain below the MS, however, where mid/far-IR detections are rare or nonexistent (e.g., Wuyts et al. 2011a). Eales et al. (2015, 2017) have shown that far-IR-based SFRs in the near-IR-selected, volume-limited *Herschel* reference survey in the local Universe (Boselli et al. 2010) exhibit a much more gradual transition from active star formers to passive galaxies. The sharp dichotomy observed in optically or UV-selected samples could thus be somewhat misleading, perhaps due to variations in dustiness and errors in SFRs based on spectral energy distributions.

Figure 2

sSFR = SFR/M_* (Gyr^{-1}) (*a,b*) as a function of $\log(1 + z)$ at $\log(M_*/M_\odot) = 10.7$ and (*c,d*) as a function of $\log(M_*)$ for $z = 1.5$. The color distributions represent the distribution of galaxies in the 3D-HST survey on a linear scaling (Brammer et al. 2012, Skelton et al. 2014, Momcheva et al. 2016). (*a,c*) 3D-HST galaxies with $\log(M_*/M_\odot) = 10$–11.7 and $\log(\delta MS) = \pm0.6$, which have individual 24-μm *Spitzer* detections or 70-μm, 100-μm, or 160-μm *Herschel* detections, so that an IR+UV luminosity can be computed (Wuyts et al. 2011a). (*b,d*) Galaxies in the range $\log(M_*/M_\odot) = 9$–10 and galaxies across the entire mass range with only an SED-based SFR, typically resulting in underestimated SFRs, which is particularly relevant at high z, low $\log(M_*)$, and below the MS. We use the Speagle et al. (2014) MS prescription (Equation 1) to correct all galaxies to the same mass of $\log(M_*/M_\odot) = 10.7$ in panels *a* and *c* and to the same redshift ($z = 1.5$; $t_c = 4.7$ Gyr) in panels *b* and *d*. The solid magenta, dashed gray, and solid black lines denote the Speagle et al. (2014), Whitaker et al. (2012), and Whitaker et al. (2014) prescriptions of the MS, respectively. Abbreviations: MS, main sequence; SED, spectral energy distribution; SFR, star-formation rate; sSFR, specific SFR. Figure adapted and updated from Tacconi et al. (2018, figure 1).

In **Figure 2** and for the rest of this review (see also Tacconi et al. 2018), we use the MS definition of Speagle et al. (2014):

$$\log\left[\text{sSFR(MS}, z, M_*)(\text{Gyr}^{-1})\right] = [-0.16 - 0.026 \times t_c(\text{Gyr})] \times [\log M_*(M_\odot) + 0.025]$$
$$- [6.51 - 0.11 \times t_c(\text{Gyr})] + 9,$$
$$\text{with } \log t_c(\text{Gyr}) = 1.143 - 1.026 \times \log(1 + z) - 0.599 \times \log^2(1 + z)$$
$$+ 0.528 \times \log^3(1 + z).$$

1.

Here, t_c (Gyr) is the cosmic time (see footnote 2). The Speagle et al. (2014) prescription is applicable over a wide range of redshifts, $z = 0$–5, and a wide range of stellar masses, $\log(M_*/M_\odot) =$ 9.0–11.8, optimal for cold gas evolution comparisons. The main disadvantage of the Speagle et al. (2014) definition is that it is calibrated mostly on SED-based SFRs, which, as discussed above, tend to be lower than UV+IR-based SFRs. Except for these issues, the Speagle et al. (2014) formula is very similar to the relations proposed by Whitaker et al. (2012, 2014).

1.4. Structure of Main Sequence Galaxies

Förster Schreiber & Wuyts (2020) present a comprehensive review of the physical properties of MS SFGs; here, we summarize some key results from the last several years. At all redshifts up to the ($z \sim 2$) peak of the galaxy or SFR, MS SFGs have disky, exponential rest-frame optical-light distributions with Sersic indices, $n_{Sersic} \sim 1$–2 (Wuyts et al. 2011b), despite the often clumpy and irregular appearance of $z > 1$ SFGs in the rest-frame UV. The majority of massive [$\log(M_*/M_\odot) > 10$] SFGs are rotationally supported disks (e.g., Wisnioski et al. 2015, 2019; Simons et al. 2017). With increasing redshift, the fraction of lower-mass SFGs with dispersion-dominated kinematics increases, suggesting that these systems are not settled, equilibrium disks (Kassin et al. 2012, Newman et al. 2013, Simons et al. 2017, Wisnioski et al. 2019). There are also subgalactic, random motions due to unresolved streaming and a floor of galaxy-wide local turbulence (Elmegreen & Scalo 2004, Scalo & Elmegreen 2004). In star-forming ionized gas, the 1D rms velocity dispersion increases with redshift as σ_0 (km s^{-1}) $\sim a + b(1 + z)$ ($a \sim b \sim 10$–11 km s^{-1}) (Übler et al. 2019; see also Förster Schreiber et al. 2006, 2009; Kassin et al. 2007, 2012; Shapiro et al. 2008; Epinat et al. 2012; Newman et al. 2013; Wisnioski et al. 2015; Stott et al. 2016; Simons et al. 2017; Bezanson et al. 2018). The $z = 0$ value of the velocity dispersion in molecular gas is smaller [$a \sim 0$, $\sigma_0(z = 0)_{mol} \sim 10$ km s^{-1}], but the slope with redshift is the same as for the ionized gas (Übler et al. 2019), so that at high z ionized and molecular gas dispersions are broadly comparable. The tightness and constant shape of the MS suggest that at any cosmic epoch SFGs grow along the sequence in an equilibrium of gas accretion, star formation, and gas outflows (Bouché et al. 2010, Davé et al. 2012, Lilly et al. 2013, Peng & Maiolino 2014; see also Section 4.3).

Many recent studies have attempted to understand the origin and evolution of the MS by focusing on molecular gas studies of galaxies at different redshifts (e.g., Bouché et al. 2010; Daddi et al. 2010a,b; Genzel et al. 2010, 2015; Tacconi et al. 2010, 2013, 2018; Davé et al. 2011a,b, 2012; Lagos et al. 2011, 2012, 2015; Fu et al. 2012; Lilly et al. 2013; Scoville et al. 2016, 2017; DeCarli et al. 2016, 2019). For more details, see Sections 2–4.

2. ESTIMATING THE COLD MASS CONTENT OF GALAXIES

2.1. The CO Line Luminosity Method

Observations of GMCs in the Milky Way and nearby galaxies have established that the integrated flux of ^{12}CO millimeter rotational lines can be used to infer molecular gas masses, although the CO molecule makes up only a small fraction ($\sim 10^{-4}$) of the entire gas mass. The CO lower rotational lines (1–0, 2–1, 3–2) are almost always very optically thick ($\tau_{CO} \sim 10$; Dickman et al. 1986, Solomon et al. 1987, Bolatto et al. 2013) because the CO emission arises in moderately dense [volume densities $<n(H_2)> \gtrsim 200$ cm^{-3}; column densities $N(H_2) \sim 10^{22}$ cm^{-2}] GMCs of kinetic temperature 10–50 K. Dickman et al. (1986) and Solomon et al. (1987) have shown that in this virial regime, or when the emission comes from a cloud ensemble with similar mass and size and

spread in velocity by galactic rotation (cloud counting), the integrated line CO line luminosity,

$$L'_{\text{CO}} = \int_{\text{source}} \int_{\text{line}} T_R \, dv \, dA \, \left(\text{in K·km·s}^{-1}\text{·pc}^2\right),$$

α_{CO}: the CO-to-H$_2$ conversion factor

is proportional to the total gas mass in the cloud or galaxy. Here, T_R is the Rayleigh–Jeans source brightness temperature as a function of Doppler velocity v. In this regime, the total molecular gas mass (including a 36% mass correction for helium) depends on the observed CO J →J–1 line flux $F_{\text{CO J}}$, source luminosity distance D_L, redshift z, and observed line wavelength $\lambda_{\text{obs J}} = \lambda_{\text{rest J}}(1 + z)$ as (Solomon et al. 1997)

$$M_{\text{molgas}}/M_\odot = \alpha_{\text{CO 1}} \times L'_{\text{CO 1}}$$
$$= 1.58 \times 10^9 \left(\frac{\alpha_{\text{CO 1}} \times R_{1J}}{\alpha_0}\right) \times \left(\frac{F_{\text{CO J}}}{\text{Jy km s}^{-1}}\right) \times (1 + z)^{-3} \times \left(\frac{\lambda_{\text{obs J}}}{\text{mm}}\right)^2 \times \left(\frac{D_L}{\text{Gpc}}\right)^2. \quad 2.$$

Here, $\alpha_{\text{CO 1}}$ is the empirical conversion factor to transform the observed quantity (CO luminosity in the 1–0 transition) to the inferred physical quantity (molecular gas mass), and R_{1J} is the ratio of the 1–0 to the J → J–1 CO line luminosity: $R_{1J} = L'_{\text{CO 1-0}}/L'_{\text{CO J – (J–1)}}$.

2.1.1. From conversion factor to conversion function. The CO conversion factor is expected to depend on several physical parameters (Narayanan et al. 2011, 2012; Feldmann et al. 2012a,b). In the virial/cloud counting model, α depends on the ratio of the square root of the average cloud density $\langle n(\text{H}_2)\rangle$ and the equivalent Rayleigh–Jeans brightness temperature, T_{RJ}, of the CO transition J→J–1. Because of photodissociation of CO by UV photons in the outer cloud layers, it also increases inversely with metallicity Z (cf. Leroy et al. 2011, Genzel et al. 2012, Bolatto et al. 2013), such that

$$\alpha_{\text{CO J}} = \alpha_0 \times \zeta \left(\frac{\langle n(\text{H}_2)\rangle^{1/2}}{T_{\text{RJ}}}\right) \times \chi(\text{Z}).$$

The functions χ and ζ are discussed in Sections 2.1.2 and 2.1.4, below. In the Milky Way, nearby SFGs with near-solar metallicity, and dense star-forming clumps of lower-mass and lower-metallicity galaxies, the empirical CO 1–0 conversion factor $\alpha_{\text{CO 1}}$ has been determined through dynamical, dust, and γ-ray calibrations (see Bolatto et al. 2013 for a review). These are broadly consistent with a single value of $\alpha_{\text{CO1}} = \alpha_0 = 4.36 \pm 0.9$ [M$_\odot$ (K·km·s^{-1}·pc^2)$^{-1}$], equivalent to $X_{\text{CO}} = N(\text{H}_2)/(T_{\text{RJ}=1}\Delta v) = 2 \times 10^{20}$ [cm^{-2} (K·km·s^{-1})$^{-1}$] (Strong & Mattox 1996; Dame et al. 2001; Grenier et al. 2005; Bolatto et al. 2008, 2013; Abdo et al. 2010; Ostriker et al. 2010; Leroy et al. 2011). Scoville et al. (2014, 2016, 2017) advocate for $\alpha_0 = 6.5$ (50% larger than the value above) on the basis of a virial analysis of Milky Way GMCs. Throughout this review, we adopt $\alpha_0 = 4.36$, consistent with Daddi et al.'s (2010a,b) value of $\alpha_{\text{CO}} = 3.6 \pm 0.8$, which includes H I and helium.

2.1.2. Metallicity dependence of the conversion factor. For galaxies with subsolar gas-phase metallicity, the conversion factor and metallicity are inversely correlated because CO is photodissociated (and the atomic carbon is photoionized) in an increasing fraction of the molecular hydrogen gas column. The result is that the H$_2$ gas is deficient (dark) in CO (Wilson 1995, Arimoto et al. 1996, Israel 2000, Wolfire et al. 2010, Leroy et al. 2011, Genzel et al. 2012, Bolatto et al. 2013, Nordon & Sternberg 2016). Motivated by theoretical research on CO

photodissociation in clouds with a range of hydrogen densities and UV radiation field intensities, but with a constant hydrogen column (Wolfire et al. 2010), Bolatto et al. (2013) proposed that $\chi(Z) = 0.67 \times \exp\{0.36 \times 10^{-[12 + \log(O/H) - 8.67]}\}$. Here, $Z = 12 + \log(O/H)$ is the gas-phase oxygen abundance in the Galaxy on the Pettini & Pagel (2004) calibration scale, with a solar abundance of $Z_\odot = 8.67$ (Asplund et al. 2004). The relation assumes an average GMC hydrogen column density of 9×10^{21} cm^{-2} or a mass surface density of 100 M$_\odot$ pc^{-2}. Genzel et al. (2012) combined local (Leroy et al. 2011) and high-z empirical evidence to derive a second fitting function, $\chi(Z) = 10^{-1.27 \times [12 + \log(O/H) - 8.67]}$. For metallicities above $0.5 \times Z_\odot$, the two fitting functions yield values within ± 0.2 dex of each other, but the former increases more strongly at low Z. Other studies (Israel 1997; Wolfire et al. 2010; Schruba et al. 2011; Feldmann et al. 2012a,b; Sargent et al. 2014) have found similar metallicity dependencies. Bisbas et al. (2015) have pointed out that in galaxies with enhanced cosmic-ray rates (which would be correlated with enhanced SFRs) CO can also be destroyed deep within clouds (Bialy & Sternberg 2015) and might significantly affect the spatial distribution of CO in a galaxy and, thus, effectively, the conversion factor.

2.1.3. CO ladder excitation dependence of the conversion factor. Observations of CO rotational ladders in near-MS galaxies between $z = 0$ and $z = 3$ yield median correction factors of $R_{J1} = 1.3, 1.8,$ and 2.4 for the 2–1, 3–2, and 4–3 transitions, respectively (Weiss et al. 2007, Dannerbauer et al. 2009, Riechers et al. 2010, Ivison et al. 2011, Bauermeister et al. 2013, Bothwell et al. 2013, Combes et al. 2013, Aravena et al. 2014, Daddi et al. 2015). This excitation correction entails a combination of the Planck correction (for a finite rotational temperature), as well as a correction for subthermal population in the upper rotational levels. While these corrections could vary from galaxy to galaxy, their scatter is unlikely to be greater than ± 0.1 dex, as judged from recent data sets.

2.1.4. Density–temperature dependence of the conversion factor. This leaves the function $\zeta[(< n(H_2) >)^{1/2}/T_{RJ}]$, which is correlated with the SFR at a given mass and redshift, that is, the vertical location in the stellar mass–SFR MS plane (Elbaz et al. 2011, Gracia-Carpio et al. 2011, Lada et al. 2012, Nordon et al. 2012). The average hydrogen gas density and temperature in Milky Way GMCs is $n \sim 100$ and $T_{R1} \sim 15$ K, such that $\zeta \sim O(1)$. Interestingly, in the much denser but also much warmer gas in extreme luminous and ultraluminous IR galaxies (LIRGs and ULIRGs) in the local Universe, or in gas-rich SFGs at high z, ζ may be broadly similar to that in the Milky Way. From a comparison of the galaxy-integrated data in the three different tracers discussed in Section 3.2, below, this correction factor appears to be unity within ± 0.15 dex within an offset $\delta MS = \log\{SFR/[SFR(MS, z)]\}$ of ± 1.3 of the MS line at redshift z, SFR(MS, z). With these uncertainties in the assumptions, calibrations, and systematics, the uncertainty of CO-based gas masses near the MS is likely no smaller than ± 0.2 dex, and increasing away from the MS.

The cosmic microwave background (CMB), $T_{CMB} = 2.725 \times (1 + z)$, can become increasingly important for molecular excitations and radiative transport of molecular lines, with increasing redshift (see Carilli & Walter 2013, their section 2.10). The line emission is in the foreground of the CMB. Since the extended CMB continuum is resolved by the millimeter interferometers, the on-source line emission is lower than without the CMB, unless the line is optically thick. Likewise, for optically thin gas, the CMB increases the molecular excitation source function by $\delta S_{CMB} = \{\exp[h\nu(J, z)/kT_{CMB}] - 1\}^{-1}$. Since molecular gas densities and temperatures on galaxy-integrated scales increase with redshift, the effects of the CMB overall are modest (5–20%) in terms of the source functions in the J = 2 to 4 CO transitions and for $z < 3$, and they are neglected in the following discussion. This simplification may not be appropriate at high z.

2.2. The Dust Method: Far-IR Spectral Energy Distributions

With the *Herschel* space observatory (2009–2013), several groups assembled deep far-IR continuum surveys with the PACS and SPIRE instruments (ATLAS, Eales et al. 2010; PEP, Lutz et al. 2011; GOODS-*Herschel*, Elbaz et al. 2011; HerMES, Oliver et al. 2012). Magdis et al. (2011, 2012b), Magnelli et al. (2014), Santini et al. (2014), Béthermin et al. (2015), and Berta et al. (2016) established 100- to 500-μm far-IR SEDs from individual galaxies or from stacking PACS and SPIRE photometry in several of the cosmological deep field surveys (e.g., GOODS-N/S and COSMOS) for SFGs in the redshift range 0.1–2.5. As an example, Magnelli et al. (2014) binned their data onto a 3D grid in z, SFR, and M_* and stacked the photometry in each bin. They then fitted model SEDs from the library of Dale & Helou (2002), for which dust temperatures were established from single optically thin, modified blackbody fits with emission index $\beta = 1.5$. From these stacked SEDs, Magnelli et al. derived dust masses from Draine & Li (2007) and modified blackbody models (Genzel et al. 2015, Berta et al. 2016). Magdis et al. (2012b), Santini et al. (2014), and Béthermin et al. (2015) obtained similar results based on different galaxies and somewhat different methodologies. Berta et al. (2016) present a comprehensive analysis of uncertainties in *Herschel*-based dust masses. A comparison of these different results shows that the systematic uncertainties in dust masses obtained from this far-IR technique is probably ±0.25 dex.

The conversion to gas masses requires a metallicity-dependent dust-to-gas ratio correction, which also enters the redshift evolution through the redshift dependence of the mass–metallicity relation (e.g., Béthermin et al. 2015). Following Magdis et al. (2012b), Draine & Li (2007) model dust masses are converted to (molecular) gas masses by applying the Leroy et al. (2011) metallicity-dependent gas-to-dust ratio fitting function for $z \sim 0$ SFGs:

$$\delta_{\rm gd} = M_{\rm molgas}/M_{\rm dust} = 10^{\{+2 - 0.85 \times [12 + \log({\rm O/H}) - 8.67]\}},$$

where $12 + \log({\rm O/H})$ is, again, the gas-phase oxygen abundance [see also Draine et al. 2007 for dust-to-gas with metallicity scalings of the SINGS nearby galaxy sample, and Galametz et al. 2011 or Rémy-Ruyer et al. 2014 for lower-metallicity galaxies down to $12 + \log({\rm O/H}) = 8.0$].

The gas column densities in the Leroy et al. (2011) recipe refer to the sum of molecular and atomic gases, but we are interested in the molecular gas (H_2)-to-dust ratio. From WISE/*Herschel* mid- and far-IR data and IRAM 30-m CO 2–1 observations in 78 nearby SFGs in the stripe 82 region, Bertemes et al. (2018) find a linear relation between CO-based (see above) and far-IR dust-based columns and argue that for the molecular gas-to-dust ratio, $\delta_{\rm gd}({\rm molgas}) \sim 67$, with little dependence on metallicity. In our analysis, we use the gas-to-dust ratio analysis by Bertemes et al. (2018).

2.3. The Dust Method: 1-mm Continuum Luminosity

Scoville et al. (2014, 2016, 2017) have proposed that a single-frequency, broadband measurement in the Rayleigh–Jeans tail of the dust SED (for instance, at 345 GHz, ~1 mm) is sufficient to establish dust and gas masses. This ansatz is justified if the emission is optically thin and the variation of the mass-weighted dust temperature on galactic scales is small. This proposal is broadly consistent with the slow changes of average $T_{\rm dust}$ with redshift and sSFR near the MS in the stacked *Herschel* data (Magnelli et al. 2014), but higher and a wider range of temperatures are observed in high-surface-brightness galaxies, such as local ULIRGs (see Section 5). On the basis of SCUBA observations of a subset of the sample of $z \sim 0$ disks from Draine et al. (2007), Scoville et al. also argue that the molecular gas-to-dust ratio does not vary significantly with

metallicity, in agreement with the findings of Bertemes et al. (2018). To calibrate the dust opacity at the observing frequency ν_{obs}, Scoville et al. use a variety of CO observations of local normal galaxies and LIRGs, as well as high-z SMGs, and the assumptions of $T_0 = 25$ K, $\alpha_0 = 6.5$, and $\delta_{gd} = 150$ to determine the zero point $\alpha_{dust0}(352 \text{ GHz}) = (L_{dust}/M_{molgas})|_{352 \text{ GHz}} = 6.7 \times 10^{19}$ erg (s·Hz·$M_\odot$)$^{-1}$ (see table 5 of Scoville et al. 2016 for references), yielding

$$\left(\frac{M_{molgas}}{1 \times 10^{10} M_e} \right) = \left(\frac{S_{\nu_{obs}} D_L^2}{\text{mJy Gpc}^2} \right) \times (1+z)^{-(3+\beta)} \times \left(\frac{\nu_{obs}}{352 \text{ GHz}} \right)^{-(2+\beta)} \times \left(\frac{6.7 \times 10^{19}}{\alpha_{dust,0}} \right) \times \left(\frac{\delta_{gd}}{150} \right). \quad 3.$$

For the frequency dependence of the dust opacity, Scoville et al. adopt $\beta = 1.8$. Kaasinen et al. (2019) recently recalibrated this method through observations of both CO (1–0) and 850-μm dust emission in 12 $z \sim 2$ SFGs, finding good agreement with the calibration of Equation 3.

In our analysis below (based on $\alpha_0 = 4.36$ and $\delta_{gd} = 67$), we find the best agreement between the available 1-mm dust measurements and the far-IR and CO observations for $\alpha_{dust,0} = 8 \times 10^{19}$, very close to the value proposed by Scoville et al. This is because, to first order, the larger CO conversion factor used by Scoville et al. compensates for their larger adopted gas-to-dust ratio.

2.4. Molecular Hydrogen and Other Molecular Lines

Molecular hydrogen, H_2, comprises most of the mass of GMCs. Yet because it lacks an electric dipole moment, the rotational transition probabilities are very small, and the line emission is weak. Moreover, the low moment of inertia results in a wide spacing of the rotational states. The J = 2–0 transition is at 28 μm, equivalent to a level spacing of 510 K. As a result, the rotational transitions are sufficiently excited only in very warm star-forming regions or in shocked and UV-irradiated gas (Parmar et al. 1991, Richter et al. 1995). In cases of bright background sources, H_2 rovibrational transitions at 2 μm are detectable in absorption (Lacy et al. 1994, 2017). H_2 can also be detected in the far-UV Lyman–Werner electronic bands in absorption against background stars or AGN (e.g., Shull et al. 2000; Rachford et al. 2002, 2009; Tumlinson et al. 2002; Gillmon et al. 2006). However, the far-UV observations can sample only the diffuse ISM or translucent clouds. In general, H_2 spectroscopy is not practical for surveying the cold gas content of galaxies.

While the lower CO rotational transitions probe moderately dense and cool gas, it could be of substantial interest to pick out the denser and more excited gas components in galaxies. For instance, the lower rotational transitions of HCN (Lee et al. 1990) can be bright in dense star-forming clouds. Gao & Solomon (2004), Vanden Bout et al. (2004), and Gao et al. (2007) pioneered HCN observations in local (U)LIRGs and some very bright or lensed distant SFGs and SMGs. They found a linear relationship between HCN and far-IR luminosities as well as 3–10-fold-enhanced HCN/CO flux ratios in these extreme starbursts in comparison to normal spirals; they proposed that this excess is due to a highly elevated dense gas fraction. To date there have been no systematic studies of HCN (or other high-dipole-moment molecules) at high z, but in principle these are now feasible with the capabilities of ALMA and NOEMA. Regions where CO is photodissociated by UV photons or destroyed by cosmic rays might instead be studied in atomic or ionized carbon fine-structure lines (Stacey et al. 2010, Tomassetti et al. 2014, Herrera-Camus et al. 2015, Bisbas et al. 2017, Papadopoulos et al. 2018).

2.5. Three Measurement Approaches

There are three approaches to studying the cosmic gas evolution. First, the pointed source approach starts with a flux/luminosity or mass-selected parent sample, with well-established and

homogeneously calibrated galaxy parameters (M_*, SFR, R_e). The SDSS sample is the prime example for $z = 0$ (Brinchmann et al. 2004; Saintonge et al. 2011a,b). At $0 < z < 3$, the CANDELS/3D-HST surveys in the GOODS-N/S, EGS, COSMOS, and UDS fields are currently the most powerful such imaging samples (Grogin et al. 2011, Koekemoer et al. 2011, Brammer et al. 2012, Skelton et al. 2014, Momcheva et al. 2016). An appropriately selected subset of these parent samples then serves as a benchmark for the entire parent population. To the extent possible, CANDELS/3D-HST contains mid-IR (*Spitzer*/WISE) or far-IR (*Herschel*) photometry, such that SFRs based on IR data are included (Wuyts et al. 2011a). All of the leading pointed surveys of the last decade, such as PHIBSS, have emphasized massive galaxies, mainly to avoid large and uncertain corrections for subsolar metallicities. Far-IR/SMG surveys (e.g., SHADES, Mortier et al. 2005; LESS, Weiss et al. 2009; *Herschel*-ATLAS, Eales et al. 2010) are generally much smaller but pick out dusty massive SFGs and SFGs above the MS. The hidden assumption of the pointed source approach is that the parent imaging survey contains essentially all relevant objects in the sky, so that only the quantity gas mass must be established. Rodighiero et al. (2011, 2015) show that this assumption is valid to at least $z \sim 3$.

Second, the deep field scanning approach usually selects a region on the sky, typically several square arcminutes, for which multiband data may be available, and blindly images the region for line or continuum emission by stepping or scanning. Detections are then classified by reliability and matched to existing multiband data (e.g., Decarli et al. 2014, 2016; Aravena et al. 2016, 2019; Walter et al. 2016; Dunlop et al. 2017; Pavesi et al. 2018; González-López et al. 2019; Riechers et al. 2019). This technique detects already-known galaxies that happen to be in the survey field and, as such, is equivalent to the pointed method. In addition, it is capable of detecting galaxies that were not present in the standard optical/UV/near-IR imagery, so it is considered less biased than the pointed method. As has been demonstrated by the highly productive HST deep fields (e.g., Williams et al. 1996, Giavalisco et al. 2004, Beckwith et al. 2006), the deep field technique is preferred if the source density is high enough that source multiplicity per pointing (or per primary telescope beam for interferometers) is high.

Published studies permit comparison of the current efficacies of these two methods. The PHIBSS1 and 2 CO surveys at NOEMA of EGS and CANDELS/3D-HST galaxies have average source detection times of 25 and 12 h ($>4\sigma$ per detected galaxy, including calibration and overheads). The improvements are due to increases in the number of antennas and the quality of receivers between 2008 and 2018. Extrapolating to the NOEMA 12 array and to ALMA yields an average detection time for CO emission ($>4\sigma$) of $\log(M_*/M_\odot) = 10.3$–11.3 galaxies at $z = 0.7$–2 of 4–6 h (NOEMA 12) and 1.2–1.7 h (ALMA 43), including calibration and overheads. For the HUDF-S ALMA-ASPECS $z = 1$–2.6 deep field CO project (Aravena et al. 2019, DeCarli et al. 2019), the average detection rate is 1 galaxy (with a known optical counterpart) per 4 h of ALMA on source integration time. Most of the Aravena detections are at $z \sim 1$–2.6 and $\log(M_*/M_\odot) = 10$–11.2, comparable to the assumptions above; there are two sources below $\log(M_*/M_\odot) = 10$. This detection rate is 2.7 times slower than ALMA pointed observations, probably caused by extra overheads in the deep field approach combined with the low surface density of massive SFGs. The number of line candidates (without known counterparts) in all deep field projects is approximately twice as high as the number with counterparts, so the detection rate is 1 galaxy per 2 h, assuming that all these other detections are real. This detection rate is comparable to the ALMA pointed efficiency but requires [for HST, *James Webb Space Telescope* (JWST), etc.] follow-up to establish the basic galaxy parameters. Given the cosmic volume covered by ASPECS 3 mm, the number of detected sources (including less-secure source candidates) is approximately what is expected from the Madau & Dickinson (2014) mass functions at $z = 1$–2.5 at high stellar masses. We conclude that the deep field CO detection efficiency (of ALMA) in the $\log(M_*/M_\odot) = 10$–11.2 bin is

comparable to or slightly faster than the NOEMA pointed observations but approximately one-half to one-third as fast as pointed ALMA observations, assuming similar conditions. The number of low-mass galaxies [in the $\log(M_*/M_\odot) = 9$–10 bin] should be an order of magnitude greater than the few sources actually detected, indicating that the CO detections are substantially incomplete in that lower-mass bin, and making the deep field CO technique much less efficient than it could be in principle.

The situation is comparable for 1-mm dust observations. The detection rate at 1 mm for pointed observations at ALMA is 1 galaxy per 10 min in the $\log(M_*/M_\odot) = 10$–11.2 bin and between $z = 1$ and $z = 2.6$ (e.g., Scoville et al. 2016, Tadaki et al. 2017, Cowie et al. 2018). The Dunlop et al. (2017) 1-mm deep field study detected 1 galaxy in these ranges per 1.5 h and only 3 galaxies below 10^{10} $M_\odot$, whereas the expectation from the Madau & Dickinson (2014) mass functions is ∼46. The dust technique is also incomplete at low masses.

The third method is intensity mapping, the measurement of the wavelength power spectrum of the distant molecular medium without spatial imaging (Righi et al. 2008, Lidz et al. 2011, Mashian et al. 2015, Li et al. 2016, Breysse & Rahman 2017). This technique derives from similar efforts to detect the power spectrum of 21-cm HI in the reionization epoch (PAPER, Ali et al. 2015; HERA, DeBoer et al. 2017). Keating et al. (2016) have presented the first constraints of the CO power spectrum. New experiments slated to start in the next few years should provide many new results from this technique (e.g., Kovetz et al. 2017).

All three techniques are challenged by the strong metallicity dependence of the CO conversion function $\chi(Z)$ below $Z \leq 0.5\,Z_\odot$, due to CO photodissociation by far-UV radiation (e.g., Nordon & Sternberg 2016), and by the metallicity-dependent gas-to-dust ratio. At $z \sim 2$, a galaxy of mass 10^{10} $M_\odot$ has $Z \sim 0.4\,Z_\odot$ and two-times-fainter CO lines than a massive SFG, and a 10^9 $M_\odot$ SFG has $Z \sim 0.13\,Z_\odot$ and eight-times-fainter CO lines. This problem gets worse with redshift, such that it would be extremely difficult to detect CO emission in low-mass $z = 2$–8 SFGs. Metallicity effects on the dust continuum emission are more uncertain (see Sections 2.2 and 2.3).

3. GALAXY-INTEGRATED SCALING RELATIONS

3.1. Depletion Time as the Primary Parameter of Gas Evolution

Given the close connection between molecular gas evolution and the cosmic star-formation history and star-formation MS, a very important quantity is the ratio of the molecular gas mass to the SFR. This quantity is called the molecular depletion timescale, $t_{\mathrm{depl}} = M_{\mathrm{molgas}}/\mathrm{SFR}$ (Gyr), which expresses the time in which a molecular gas reservoir would be depleted by current star-formation activity, without considering any mass return to the ISM from stellar winds and supernovae. The inverse of the depletion timescale, $\varphi_{\mathrm{depl}} = 1/t_{\mathrm{depl}}$, is often described in the literature as an efficiency (although it has units of 1/time), where $\varphi_{\mathrm{depl}} = \varepsilon_{\mathrm{ff}}/t_{\mathrm{ff}}$ and $\varepsilon_{\mathrm{ff}}$ is the efficiency of star formation per free-fall time or per galaxy dynamical time (see also Section 3.5). The depletion time is the ratio of abscissa and ordinate in galaxy-integrated versions of the Kennicutt–Schmidt (KS) scaling relation between (molecular) gas and SFR (Kennicutt 1998, Kennicutt & Evans 2012). If t_{depl} at a given z does not vary with SFR, then the slope of the KS relation, N_{KS}, is equal to unity (Bigiel et al. 2008; Leroy et al. 2008, 2013; Daddi et al. 2010b; Genzel et al. 2010; Kennicutt & Evans 2012). Once the dependence of the depletion timescale on redshift and the key galaxy parameters (M_*, SFR, R_e) are determined, the cosmic evolution of the ratio of gas to stellar mass, $\mu_{\mathrm{molgas}} = M_{\mathrm{molgas}}/M_*$, follows automatically, since $\mu_{\mathrm{molgas}} = t_{\mathrm{depl}} \times \mathrm{sSFR}$, and finally, $f_{\mathrm{molgas}} = \mu_{\mathrm{molgas}}/(1 + \mu_{\mathrm{molgas}})$.

Genzel et al. (2015), Tacconi et al. (2018), and Scoville et al. (2017) have demonstrated that the dependencies of t_{depl} and μ_{molgas} on the physical parameters can be separated as products of power

t_{depl}: the molecular gas depletion timescale, $M_{\mathrm{molgas}}/\mathrm{SFR}$

μ_{molgas}: M_{molgas}/M_*, the molecular gas–to–stellar mass ratio

f_{molgas}: $M_{\mathrm{molgas}}/(M_{\mathrm{molgas}} + M_*)$, the molecular gas fraction

laws that are functions of $(1 + z)$, of offset from the MS, of δMS (perpendicular to the MS), and of M_* (along the MS):

$$t_{\mathrm{depl}} = t_0 \times (1 + z)^A \times [\mathrm{SFR/SFR(MS}, z, M_*)]^B \times (M_*/5 \times 10^{10} \mathrm{M}_\odot)^C. \qquad 4.$$

As we show below, studies of cosmic cold gas evolution agree that the galaxy-integrated depletion timescale depends mainly on redshift and offset from the MS (at a given z). There is little or no dependence on galaxy mass, size, or environment. Since more than 90% of the cosmic SFR occurs on the MS (Rodighiero et al. 2011, 2015), the single-parameter sequence $t_{\mathrm{depl}}(z)|_{\mathrm{MS}}$ can be used as a first-order estimate to determine the cosmic evolution of cold gas, if the star-formation history is well known. We feel that this is a very important conclusion, since the measurement of a molecular gas mass of a galaxy is much more costly than determining an SFR. Currently there are a few thousand published galaxy gas mass measurements, compared with 10^6 or more SFRs.

3.2. Depletion Time Scaling Relations

To update the depletion time scaling relations of Genzel et al. (2015), Tacconi et al. (2018), and Scoville et al. (2017), we have assembled from the existing literature and the ALMA archive molecular gas mass detections ($>3.8\sigma$) for individual galaxies and stacks (see Section 2.2) for 2,052 SFGs between $z = 0$ and 5.3, $\log(M_*) = 9$ and 12.2, and δMS $= -2.6$ and $+2.2$ (assuming the Speagle et al. 2014 definition of the MS). SFRs range between $\log(\mathrm{SFR}) = -1.5$ and $+3.75$. Of the entries in this compilation,[4] 858 are based on CO (1–0, 2–1, 3–2, or 4–3) detections (see Section 2.1 for details), 724 on far-IR dust measurements (Section 2.2), and 470 on ∼1-mm dust measurements (Section 2.3). **Table 1** lists the surveys and references for this compilation. The dominant uncertainties are systematic rather than statistical uncertainties of individual measurements, which are typically lower than ±0.1 dex. Assumptions regarding IMFs and star-formation histories dominate for stellar masses and SFRs and result in ±0.15- to ±0.25-dex uncertainties, increasing to ±0.3 dex above the MS, in the starburst regime. The various assumptions going into the derivation of CO- or dust-based molecular masses are ±0.25 dex. Some of these systematic dependencies drop out when using reduced quantities, such as sSFR or μ_{molgas}, since numerator and denominator are affected similarly.

3.2.1. Redshift scaling.
Following Tacconi et al. (2018), we first establish zero-point correction factors for each set of measurements, relative to the final average. We consider only the MS SFGs at all redshifts (δMS $= \pm0.6$) and exploit the finding that this subset varies only as a function of redshift. We then establish zero-point offsets for the various data sets (between -0.1 and $+0.27$ dex) to minimize the scatter of the $\log(t_{\mathrm{depl}})$–$\log(1 + z)$ relation. **Figure 3a** shows all the resulting MS points individually for the three gas mass determination techniques. For all three methods, the redshift trend for MS galaxies can be well fitted by a power law of slope $B = \mathrm{d}\log(t_{\mathrm{depl}})/\mathrm{d}\log(1 + z) = -0.9$ (±0.1, CO), -1.1 (±0.12, far-IR), and -1.3 (±0.32, 1 mm), where all uncertainties quoted here and below are 2σ fit errors. The combined slope for all three techniques is $B = -0.98$ (±0.06, ±0.1), where the first is the statistical uncertainty and the second is the systematic error, depending on the weighting of different data sets or on whether all data points are used, and simultaneously fitting t_0, A, B, C, and D. This value for the redshift slope is in excellent agreement with, and improves on, values from Daddi et al. (2010b), Magdis et al. (2012b), Santini

---

[4]See **Supplemental Table 1**. The list contains the basic ancillary information [z, $\log(M_*)$, $\log(\mathrm{SFR})$, $\log(\mathrm{sSFR})$, $\log(t_{\mathrm{depl}})$, $\log(\mu_{\mathrm{molgas}})$, R_e (rest frame optical)] and the zero-point offsets chosen for the input $\log(t_{\mathrm{depl}})$ and $\log(\mu_{\mathrm{molgas}})$.

Supplemental Material >

Table 1 Surveys of molecular gas and dust for galaxy evolution: sources used for gas scaling relations

Survey	Reference(s)	Method	Sources	Redshift range
xCOLDGASS[a]	Saintonge et al. 2011a,b; 2016; 2017	CO	293 detections 1 stack (nonde-tection)	$z \sim 0$
CALIFA-EDGE	Bolatto et al. 2017, Utomo et al. 2017	CO	100 detections included	$z \sim 0$
LIRGs/ULIRGs	Gao & Solomon 2004, Gracia-Carpio et al. 2008, Armus et al. 2009, Gracia-Carpio 2009, Garcia-Burillo et al. 2012	CO	90	$z \sim 0$
CO–far IR SED cross-calibration	Bertemes et al. 2018	CO, SED dust	78 CO 78 far-IR spectral energy distributions	$z \sim 0$
EGNOG	Bauermeister et al. 2013	CO	31	$z \sim 0.05$–0.5
$z \sim 0.5$ ULIRGs	Combes et al. 2011, 2013	CO	32	$z \sim 0.2$–0.9
PHIBSS[a]	Tacconi et al. 2013, 2018; Genzel et al. 2015; Freundlich et al. 2019	CO	131	$z \sim 0.5$–2.5
ASPECS	Decarli et al. 2016, 2019	CO	22	$z \sim 1$–3.5
Other high-z CO (PdBI, ALMA, NOEMA)	Daddi et al. 2010a; Genzel et al. 2015; Magdis et al. 2012a, 2017; Magnelli et al. 2012; Suess et al. 2017; Spilker et al. 2018; Tacconi et al. 2018; Übler et al. 2018; Valentino et al. 2018; Herrera-Camus et al. 2019	CO	35	$z \sim 0.5$–3.2
$z \sim 1$ starbursts	Silverman et al. 2015, 2018	CO	12	$z \sim 1.5$
SMGs[b]	Tacconi et al. 2006, 2008; Bothwell et al. 2013	CO	18	$z \sim 1.2$–4.0
High-z MS lensed SFGs	Saintonge et al. 2013	CO	7	$z \sim 1.4$–2.7
COSMOS CO–dust cross-calibration	Kaasinen et al. 2019	CO, 1-mm dust	8 CO 12 1-mm dust	$z \sim 1.7$–2.9
COSMOS PEP	Béthermin et al. 2015	FIR SED	15 stacks	$z \sim 0.75$–3.8
Herschel PEP + HerMES	Magnelli et al. 2014, Berta et al. 2016	FIR SED	510 stacks	$z \sim 0.12$–2.0
Herschel PEP + HerMES	Santini et al. 2014	FIR SED	121 stacks	$z \sim 0.12$–2.0
PHIBSS	Tacconi et al. 2018	1-mm dust[c]	7	$z \sim 1.1$–2.3
3-mm ALMA Continuum	Zavala et al. 2018	3-mm dust	20	$z \sim 1.0$–3.7
Scoville COSMOS	Scoville et al. 2016	1-mm dust	51 sources 21 stacks	$z \sim 0.9$–2.8
DANCING	Fujimoto et al. 2017	1-mm dust	102	$z \sim 0.6$–5.3
ASAGAO	Hatsukade et al. 2018	1-mm dust	23	$z \sim 1.2$–4.5
GOODS-S	Cowie et al. 2018, Franco et al. 2018	1-mm dust	68	$z \sim 0.1$–5.5
UDF	Dunlop et al. 2017	1-mm dust	12	$z \sim 0.7$–3
Tadaki 3D-HST Massive	K. Tadaki, S. Belli, A. Burkert, et al., submitted	1-mm dust	95	$z \sim 2$–2.5
Wiklind CANDELS GOODS-S	Wiklind et al. 2019	1-mm dust	25	$z \sim 0.5$–4.5

(Continued)

Table 1 (*Continued*)

Survey	Reference(s)	Method	Sources	Redshift range
Other ALMA	Genzel et al. 2015; Barro et al. 2016; Decarli et al. 2016; Hodge et al. 2016, 2019; Schinnerer et al. 2016; Magdis et al. 2017; Tacconi et al. 2018; Aravena et al. 2019; Patil et al. 2019; Sharon et al. 2019	1-mm dust	34	$z \sim 2.3$–4.8

[a]We use a 3.9σ significance cut, which results in fewer sources included compared with Tacconi et al. (2018).

[b]Not a complete list, but the same sample as used by Tacconi et al. (2018).

[c]We use "1-mm dust" to refer to all studies using the single $\sim$1-mm continuum measurement to derive molecular gas masses according to the method described by Scoville et al. (2016). The observed wavelength varies from study to study, and we refer the reader to the references listed for more details. Abbreviations: FIR, far-infrared; LIRG, luminous IR galaxy; MS, main sequence; SED, spectral energy distribution; SFG, star-forming galaxy; SMG, submillimeter galaxy; ULIRG, ultraluminous IR galaxy.

et al. (2014), Sargent et al. (2014), Béthermin et al. (2015), Genzel et al. (2015), Scoville et al. (2017), and Tacconi et al. (2018).

3.2.2. Scaling perpendicular to the main sequence. Next, we consider the variation of depletion time perpendicular to the MS line. Because of the separation ansatz of Genzel et al. (2015), Scoville et al. (2017), and Tacconi et al. (2018), it is possible to analyze all of the 2,052 data points simultaneously, after removing the redshift dependence. Doing so greatly increases the statistical robustness and the range in δMS. **Figure 3b** shows the binned averages of $t_{\mathrm{depl}}(z)$ in two bins above and one bin below the MS. There is a clear and continuous trend at all redshifts for the depletion time to decrease above and increase below the MS. The formal fit yields $C = \mathrm{d}\log(t_{\mathrm{depl}})/\delta\mathrm{MS} = -0.49\ (\pm0.03)$. This value agrees very well with those of Saintonge et al. (2011b), Huang & Kauffmann (2014), Genzel et al. (2015), Scoville et al. (2016) [$C = -0.55$ (±0.1)], and Tacconi et al. (2018), but there is some tension with the value from Scoville et al. (2017), who find a steeper dependence [$C = -0.7\ (\pm0.04)$], as well as with those from Magdis et al. (2012b), Sargent et al. (2014), and Santini et al. (2014), who find a shallower dependence [$C = -0.1$ (-0.4)].

A very important general conclusion is that all three techniques—CO line luminosity, far-IR dust SED, and 1-mm dust photometry—yield remarkably similar scaling relations, once the zero points are dealt with through cross-calibration (**Figures 3**, **4**, **5**) (Genzel et al. 2015, Magdis et al. 2017, Scoville et al. 2017, Tacconi et al. 2018). The similarity among the three enables one to search for systematic trends that may affect molecular mass measurements in any one of these three methods. The slight tension between the CO-based and dust-based estimates of C (i.e., the shallower slope for the CO-based data) might suggest a redshift dependence of α_{CO}. To alleviate this tension to first order, we average the estimates of the three techniques. Note that our method of averaging will fail if the techniques' zero points covary in similar fashion. When considering the quoted final parameter uncertainties for a given data set, one must keep in mind the coverage in the specific parameter. Using mock data sets, Tacconi et al. (2018) have shown that limited redshift coverage, in addition to small number statistics, can strongly limit the final precision of parameter estimates. Covariance between parameters must also be taken into account. As the result of these covariances and the overall calibration uncertainties, the zero points of the individual techniques are no better than ±0.2 dex.

From these cross-checks, we deduce that the slope C does not depend significantly on redshift or on δMS, as shown in **Figure 4**. Note that in this figure we have deliberately omitted a slope of
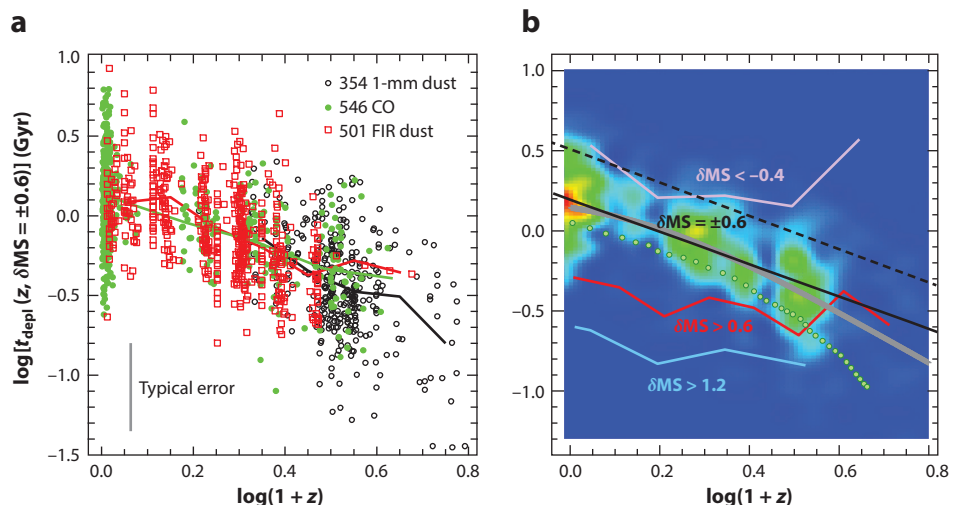
Figure 3

Molecular depletion timescale (Gyr) as a function of redshift for 1,401 MS SFGs (δMS = ±0.6) in the master sample. (*a*) CO (*green*), far-IR dust (*red*), and 1-mm dust (*black*) measurements after small zero-point corrections are applied to each data set (between −0.1 and +0.27 dex) in order to minimize the overall scatter. The green, red, and black lines are the data averages within bins of ∼0.15 dex. The scatter of the residuals around the best-fit, slope −1 power law is ±0.21, ±0.18, and ±0.26 dex for the CO, far-IR dust, and 1-mm dust measurements, respectively. For CO and far-IR data, the scatter is well within the combined statistical and systematic errors. The larger 1-mm residuals may arise in part from the fact that many galaxies have only photometric input redshifts, which can be uncertain at $z > 2$. Overall, the trend lines suggest that the three different techniques are in good to very good agreement, but at $z > 2$ the 1-mm dust data are ∼0.15–0.2 dex below either of the far-IR or CO data sets. This discrepancy is reflected in slightly different inferred slopes, $B = \mathrm{d}\log(t_{\mathrm{depl}})/\mathrm{d}\log(1 + z)$, if the data sets are considered separately. CO and far-IR data yield $B = -0.88$ (±0.1) and −1.1 (±0.16), while the 1-mm data give $B = -1.3$ (±0.32). This barely significant tension is also seen in the analyses of Tacconi et al. (2018, table 3) and Scoville et al. (2017, table 2). The quoted uncertainties are 2σ fit errors. The combined data set has $B = -0.98$ (±0.06). The zero point of the relation is $\log(t_0) = 0.21$ (±0.03), or $t_0 = 1.6$ (±0.5) Gyr. (*b*) The best fit for the combined MS data (*black*) (slope −1) is superposed on the smoothed overall distribution function, which includes all three MS data sets shown in color, and compared with the above and below MS outlier trend lines: δMS > +0.6 (*red*), δMS > +1.2 (*cyan*), and δMS < −0.4 (*pink*). These trend lines capture the [SFR/SFR(MS)]$^{-0.5}$ dependence of the depletion timescale. The thick solid gray line shows that an equally good fit to the MS data set can be obtained with an ansatz $t_{\mathrm{depl}} \sim H(z)^{-1} \sim 1.6$ Gyr $\times [0.7 + 0.3 \times (1 + z)^3]^{-1/2}$. The thick dotted green line is the redshift dependence of the depletion time, obtained by Lagos et al. (2015) from their postprocessing analysis of the EAGLE simulation. The overall shape is consistent with the observations, but the zero point is ∼0.15–0.3 dex too low. The dashed black line is the best fit from Scoville et al. (2017) [$B = -1.05$ (±0.1)]. Abbreviations: FIR, far-infrared; MS, main sequence; SFG, star-forming galaxy; SFR, star-formation rate.

−0.5 × δMS, instead of the best-fitting slope of −0.49 × δMS. This difference can be easily seen by eye as a significant positive slope of the residuals near the MS. **Figure 4** demonstrates that the residuals stay fairly flat across the entire range of δMS sampled, from below the MS (δMS ∼ −1) to the extreme starbursts above the MS (δMS ∼ +2).

On the basis of a comparison of dynamical and gas masses in ULIRGs, Scoville et al. (1997) and Downes & Solomon (1998) concluded that there is a significant drop of the CO conversion factor α_{CO} from the MS to extreme starburst galaxies ($\alpha_{\mathrm{CO}} = 0.8\ldots3$). This drop in α_{CO} has been a standard assumption in the field since then, including in our own research (e.g.,

a

b

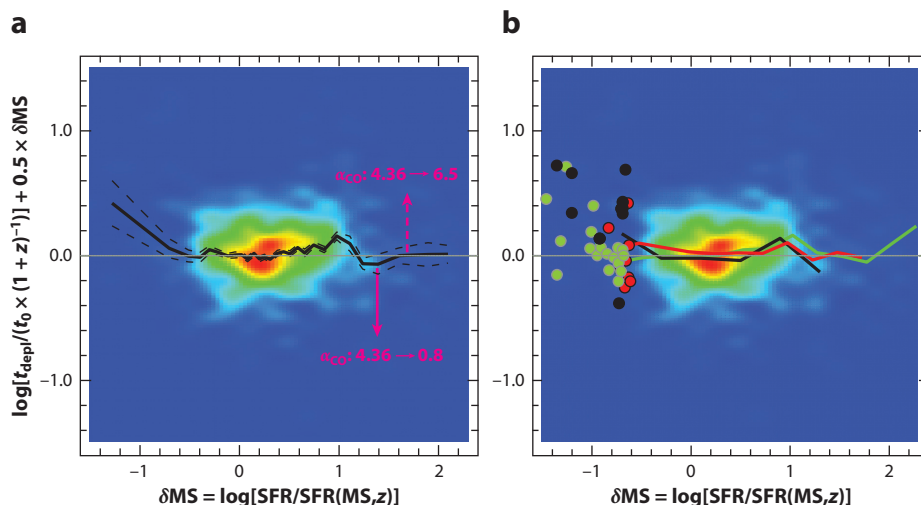## Figure 4

Residuals of depletion time as a function of MS offset, after both the redshift dependence and a slope $C = $ d $\log(t_{depl})/\delta MS = -0.5$ [note that the best-fit slope is -0.49 (± 0.03)] are removed. The color distribution contains all 2,052 data points in our master list. (*a*) The black line is the binned median of these data, and the dashed lines depict the 1σ statistical errors. The overrotation of the original data by applying a slope of -0.5 is quite visible in the residuals. The downward-pointing magenta arrow shows the change of the CO conversion factor from $\alpha_{CO} = 4.36$ at the MS to 0.8 at $\delta MS = 1.5$–2.2, as proposed by Downes & Solomon (1998). The lower masses above the MS and in ULIRGs implied by that change in α_{CO} is captured in our scaling relations by the $[SFR/SFR(MS)]^{-0.5}$ dependence of t_{depl} instead. The upward-pointing dashed arrow denotes $\alpha_{CO} = 6.5$ instead of 4.36, as proposed by Scoville et al. (2014, 2016, 2017). (*b*) Green, red, and black continuous lines mark the binned averages of CO, far-IR dust, and 1-mm dust, respectively. These findings (see also Genzel et al. 2015, Scoville et al. 2017, Tacconi et al. 2018) call into question the possible existence of a sharp transition from MS galaxies to starbursts (as a result of variations in α_{CO}) and the existence of a bimodal star-formation distribution, as proposed by Daddi et al. (2010b), Genzel et al. (2010), Magdis et al. (2012b), and Sargent et al. (2014). Likewise, any change across $\delta MS = \log[SFR/SFR(MS)]$ of the CO conversion factor should be apparent as a slope difference between the three different tracers. Such differences are not present, excluding a change in α_{CO} between MS and starburst galaxies by more than 0.15 dex. Green, red, and black circles denote CO, far-IR, and 1-mm observed galaxies below the MS, respectively. Abbreviations: MS, main sequence; SFR, star-formation rate; ULIRG, ultraluminous IR galaxy.

Genzel et al. 2010) and in that of Bolatto et al. (2013). In the papers by Genzel et al. (2015) and Tacconi et al. (2018) and in this review, the low gas masses inferred from the gas dynamics in ULIRGs, and more generally above the MS, are now encapsulated in the $\delta MS^{-1/2}$ dependence of t_{depl}, instead of a change in α_{CO}. No additional variations of α_{CO} with δMS are needed; Scoville et al. (2016, 2017) have come to the same conclusion. The overall 50%-larger gas masses proposed by Scoville et al. (2016, 2017) ($\alpha_{CO} = 6.5$ instead of 4.36) are within the systematic uncertainties of the CO zero points, but our lower values are in better agreement with the dust techniques and recent simulations (see Section 4.2.). **Figure 4** also suggests that any underlying changes in the physics of star formation as one moves from the MS line upward to the starburst populations, or down to the passive population, are most likely gradual and not bimodal, as advocated by Genzel et al. (2010), Magdis et al. (2012b), and Sargent et al. (2014).

Below the MS, the slope of the $t_{depl}(MS)$ also does not change significantly (**Figure 4a** shows the uncertainties per δMS bin). This conclusion is still uncertain because of the small number of galaxies below the MS (**Figure 4b**), and the larger scatter of the 1-mm data, but it could be
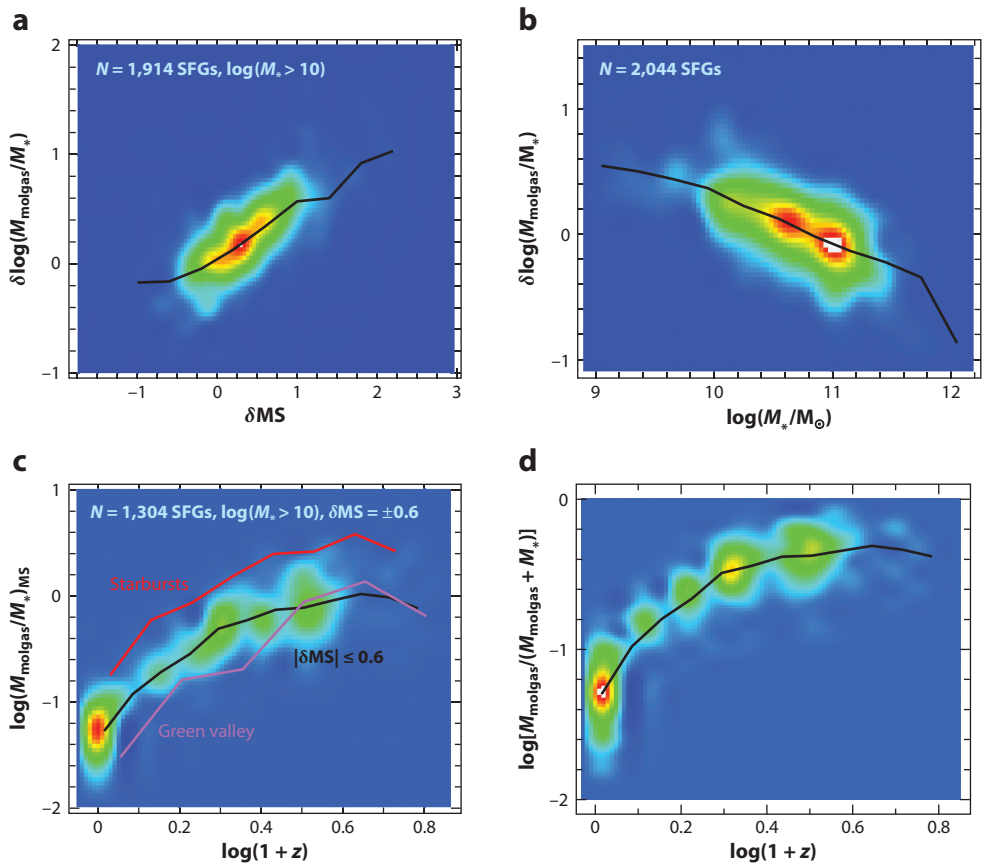
Figure 5

Scaling relations of $\mu_{gas} = M_{molgas}/M_*$ with (*a*) specific star-formation rate offset δMS and (*b*) stellar mass, (*c*) redshift, and (*d*) molecular to total mass fraction $f_{molgas} = \mu_{molgas}/(1 + \mu_{molgas})$. The smoothed distributions of the galaxies in the master set are shown underlying in color. In all panels, the thick black line represents the binned averages of the overall distribution in bins of 0.1 to 0.25 dex. In panel *c*, the black line and underlying color distribution refer to the MS (δMS = ±0.6). The red and purple lines denote the corresponding averages for starbursts (δMS > 0.6) and below-MS galaxies (δMS ← 0.4), respectively. Abbreviation: MS, main sequence.

important input into the question of whether different physical processes, such as morphological quenching, are important below the MS (Genzel et al. 2014, Suess et al. 2017, Spilker et al. 2018).

The negative slope of the t_{depl}–δMS relation ($C \sim -0.5$) affects the slope of the KS relation in samples of galaxies that contain a mixture of MS galaxies and starbursts (see Genzel et al. 2015, section 4.4). Since the KS ordinate (SFR) scales inversely with t_{depl}, starburst galaxies (δMS $\sim$ +1...+2) at a given molecular gas mass (surface density) lie above the MS galaxies, thus steepening the slope of the KS relation above unity (for constant t_{depl}). This finding plausibly explains why Kennicutt (1998) and Kennicutt & Evans (2012, figure 11) find $N_{KS} = 1.4$ and why Daddi et al. (2010b) find $N_{KS} = 1.3$–1.4 at high Σ_{gas}, whereas Bigiel et al. (2008) and Genzel et al. (2010) find $N_{KS} = 0.9$–1.2. The former authors include substantial numbers of starbursts, ULIRGs, and SMGs, while the latter focus on MS galaxies. All of these results are consistent once the dependence of t_{depl} on δMS is considered (Genzel et al. 2015).

Table 2 Fit parameters for t_{depl}[a] obtained from error-weighted, multiparameter regression[b]

Data	Parameter	N	χ_r^2	A	B	C	D
All (error weighted)	t_{depl} (Gyr)	2052	0.85	$+0.21_{0.1}$	$-0.98_{0.1}$	$-0.49_{0.03}$	$+0.03_{0.04}$

[a]See Equation 4.

[b]$\log(t_{depl})(\text{Gyr}) = A + B \times \log(1 + z) + C \times \log[\text{sSFR}/\text{sSFR}(\text{MS}, z, M_*)] + D \times [\log(M_*) - 10.7]$.

3.2.3. Dependence on other parameters.

Finally, considering the t_{depl} residuals after removing both the z and δMS dependencies, or carrying out a global overall fit, we find that the mass and radius dependence is negligible, with $D = $ d $\log(t_{depl})$/d $\log(M_*) = 0.03 \pm 0.04$ and $E = $ d $\log(t_{depl})$/d $\log(R) = 0.09 \pm 0.15$, in good agreement with the publications cited in Section 3.2.2. **Table 2** summarizes these best-fitting functions.

3.3. Scaling Relations for Ratios of Molecular to Stellar Mass

Having established the parameter dependences of $t_{depl}(z, \delta\text{MS}, M_*, R)$ we can multiply the depletion time scaling relations by Equation 1 and obtain $\mu_{molgas}(z, \delta\text{MS}, M_*) = M_{molgas}/M_*$. Alternatively, one can start with the individual molecular masses and stellar masses and then proceed by local or global fitting, with the same separation ansatz as above for the depletion time. **Figure 5** depicts the dependencies of μ_{molgas} on these three variables in graphical form, as well as the z dependence of the molecular gas fraction, $f_{molgas} = \mu_{molgas}/(1 + \mu_{molgas})$.

Ratios of molecular mass to stellar mass and molecular gas fractions broadly track the redshift dependence of sSFRs (Equation 1), since the steep $(1 + z)^3$ dependence of sSFR dominates over the slower redshift dependence of t_{depl}. As for sSFR(z), the redshift dependence of μ_{molgas} is better described by a quadratic function (Tacconi et al. 2018). MS galaxies had the largest molecular gas fractions at $z \sim 2$–3. Since $\mu_{molgas} = t_{depl} \times$ sSFR, the anticorrelation (with slope -0.5) of t_{depl} with δMS is mirrored into a positive correlation of μ_{molgas} with δMS (with slope $+0.5$). The drop in sSFR with stellar mass is fully reflected in the relation between μ_{molgas} and stellar mass. **Table 3** presents the values for the best-fitting function.

3.4. The Role of Environment

The scaling relations derived above refer to field galaxies, not members of dense, massive clusters. For a complete picture of galaxy gas properties, we must also investigate whether environment is an additional parameter regulating the scaling of the gas and star-formation properties. To date, two approaches have been used to study this effect. The first is to calculate the overdensities of galaxies in large molecular gas and dust surveys; the second is to observe galaxies located in massive clusters or protoclusters, and then compare their gas masses, gas fractions, and depletion times with those of field galaxy samples. Darvish et al. (2018) used the first method to analyze the Scoville et al. (2017) sample and a local HI-based sample from the ALFALFA survey (Haynes et al. 2011) to determine the scaling of f_{molgas} and t_{depl} with galaxy overdensity. They separate

Table 3 Fit parameters for μ_{molgas} obtained from an error-weighted, multiparameter regression[a]

Data	Parameter	N	χ_r^2	A	B	F	C	D
All (error weighted)	$\mu_{molgas} = M_{molgas}/M_*$	2,052	0.75	$+0.06_{0.2}$	$-3.33_{0.2}$	$+0.65_{0.05}$	$+0.51_{0.03}$	$-0.41_{0.03}$

[a]$\log(M_{molgas})/M_* = A + B \times [\log(1 + z) - F]^2 + C \times \log[\text{sSFR}/\text{sSFR}(\text{MS}, z, M_*)] + D \times [\log(M_*) - 10.7]$.

the samples into four density bins and match z, δMS, and M_* in each bin to those of the more than 100 galaxies in the highest-density bin to obtain a fair comparison. They find no correlation of f_{molgas} and t_{depl} with galaxy overdensity and conclude that the molecular gas content and star-formation activity of a galaxy are regulated by internal processes from $z = 0$ to $z = 3.5$, and that galaxy environment plays little or no role. A caveat is that their study does not include galaxies that are located in the densest environments, with overdensities relative to the field of ~ 100 (e.g., Tadaki et al. 2019).

Pointed studies of cluster and protocluster galaxies from $z = 0$ to $z \sim 2.5$ have come to different conclusions on the role of environment, but at present they are quite limited in sample size and possibly affected by selection effects. At $z = 0$, Kenney & Young (1989) and Koyama et al. (2017) find no effect on the molecular gas content in cluster galaxies. However, Mok et al. (2016) find an excess of gas in galaxies in dense environments, and Boselli & Gavazzi (2014) find evidence for ram pressure stripping, resulting in lower gas mass and gas fractions in dense cluster galaxies relative to field galaxies. Emerging studies at high redshift compare molecular gas contents of cluster/protocluster members with the scaling relations of Genzel et al. (2015), Scoville et al. (2017), and Tacconi et al. (2018). These studies mostly find either consistent or enhanced gas fractions relative to these field scaling relations (Lee et al. 2017, Noble et al. 2017, Rudnick et al. 2017, Hayashi et al. 2018, Tadaki et al. 2019), and some also find longer depletion times relative to those of Genzel et al. (2015), Scoville et al. (2017), or Tacconi et al. (2018) (e.g., Hayashi et al. 2018). In their study of 66 SFGs in three $z \sim 2.5$ protoclusters, Tadaki et al. (2019) find a mass-dependent environment effect. Galaxies with $10.5 < \log(M_*/M_\odot) < 11$ have higher gas fractions and longer depletion times relative to the Tacconi et al. (2018) relations, but this effect vanishes at $\log(M_*/M_\odot) > 11$. Tadaki et al. postulate that gas accretion could be accelerated in less massive galaxies and suppressed in the most massive halos, possibly because of inefficient cooling in $\log(M_{DM}/M_\odot) > 12$ halos (Rees & Ostriker 1977, Dekel & Birnboim 2006). Conclusive progress in assessing whether the galaxy environment is another parameter in the scaling relations described in Sections 3.2 and 3.3 awaits statistically significant samples of several thousand galaxies or more, spanning a wide dynamic range of galaxy overdensities.

3.5. What Sets the Depletion Time?

Figure 3b shows that the data are also well fitted by the functional form $t_{depl} = [\varepsilon_H \times H(z)]^{-1} = \varepsilon_H^{-1} \times t_H \times [0.7 + 0.3 \times (1 + z^3)]^{-1/2}$. Here, $H(z)^{-1}$ is the Hubble time at z, and $t_H = 13.98$ Gyr is the current Hubble time (**Figure 3b**). In this case, $\varepsilon_H^{-1} = 0.1$ (± 0.02).

Following Mo et al. (1998), we consider a rotationally supported baryonic disk inside a virialized dark matter halo at redshift z, where baryons and dark matter have comparable specific angular momenta, $j_{baryon} \sim j_{DM}$, and where the angular momentum parameter of the dark matter halo is λ_a. Observations of the angular momenta of low- and high-z SFGs by Romanowsky & Fall (2012), Fall & Romanowsky (2013), Burkert et al. (2016), and Swinbank et al. (2017) suggest that $j_{baryon}/j_{DM} \sim 1$ and $\lambda_a \sim 0.037$. The dynamical time of the centrifugally supported baryonic disk at the half-mass radius R_e is then

$$t_{dyn}(R_e) = R_e/v_c(R_e) = 6.15 \times 10^7 \left(\frac{j_{baryon}}{j_{DM}}\right) \times \left(\frac{\lambda_a}{0.037}\right) \times f_h \times f_{ac} \times [H(z)/H_0]^{-1}, \quad 5.$$

where the factor $f_h = v_c(R_{virial})/v_c(R_e)$ is unity for an isothermal rotation curve and ~ 1.5–2 for a Navarro–Frenk–White distribution, and $f_{ac} \leq 1$ denotes whether the halo has experienced adiabatic contraction. We adopt $f_h \times f_{ac} \sim 1.5$. Next, we assume that the depletion timescale is proportional to the Toomre time of the disk, that is, the fragmentation time of the largest unstable

THE TOOMRE–JEANS INSTABILITY CASCADE

In gas-rich, rotating-disk galaxies with disk scale length R_d, circular velocity v_c, local velocity dispersion σ_0, and gas surface density Σ_{gas}, differential rotation stabilizes cloud complexes against fragmentation on scales larger than the Toomre length $[\lambda_T = (\pi G \Sigma_{gas} R_d^2)/v_c^2 \cong R_d \times f_{gas}]$ (Toomre 1964). Between this upper stability scale and the pressure stability scale, the Jeans length $\lambda_{Jeans} \sim \sigma_0^2/G\Sigma_{gas}$, all intermediate scales are unstable, and the most rapidly growing mode has a wavelength of $2\lambda_{Jeans}$ (Toomre 1964, Binney & Tremaine 2008, Dekel et al. 2009b, Escala 2011). In finite-thickness, gas-rich, and globally Toomre-unstable disks, $Q = (\sqrt{2}\sigma_0 \times v_c)/(\pi G\Sigma_{gas} \times R_d) \leq Q_{crit} \sim 0.7$, fragmentation and cloud collapse do not occur on the local free-fall timescale but rather on the Toomre time, $t_T = (R_d/v_c) \times \{[(2Q^2)^{-1} - 1]^{-1/2}/\sqrt{2}\} \overset{Q<Q_{crit}\sim 0.7}{\to} t_{dyn} \times Q$, where $t_{dyn} = R_d/v_c$ is the galactic dynamical time (Elmegreen 1997, Silk 1997, Krumholz et al. 2012, Behrendt et al. 2015, Romeo & Mogotsi 2017).

mode, which is also the vertical oscillation time, $t_{depl} = t_T/\varepsilon_T = t_{dyn} \times Q/\varepsilon_T$ (see the sidebar titled The Toomre–Jeans Instability Cascade) (Behrendt et al. 2015). We reformulate Q, described in the sidebar as $Q = 1.41 \times (\sigma_0/v_c)/f_{molgas}$. For $\mu_{molgas} < 1$, appropriate for the MS at $z < 2$, $f_{molgas} \sim \mu_{molgas}$ to within 30–50% (**Figure 5**). Putting all this together, we can express the depletion time as

$$t_{depl} = 1.3 \times 10^8 \times \frac{\lambda_{0.037}}{\varepsilon_T} \times \left(\frac{j_{baryon}}{j_{DM}}\right) \times \left(\frac{f_h f_{ac}}{1.5}\right) \times \left(\frac{H(z)}{H_0}\right)^{-1} \times \left(\{v_c/\sigma_0\} \times \mu_{molgas}\right)^{-1} \text{(years).}$$

6.

The redshift dependence of the depletion timescale (or the slope of the KS relation on the MS) in this model is entirely in $H(z)$, in agreement with the discussion above and **Figure 3**, since $(v_c/\sigma_0) \times \mu_{molgas}$ is approximately constant and near unity as a function of redshift (Wisnioski et al. 2015, Übler et al. 2019). At a given redshift and along the MS, the depletion time should not change much, since the slow drop of gas fractions with increasing stellar mass compensates for an equivalent shallow increase of v_c/σ_0 with mass. Finally, the dependence on δMS is entirely in $\mu_{molgas} \sim \delta MS^{0.5}$ (**Table 3**) and $t_{depl} \sim \delta MS^{-0.5}$ (**Table 2**), as observed. We note, however, that the implication of the above discussion—that the average Q is lower above the MS and at high z—is strictly not consistent with the model of galaxies self-regulating to $Q \sim Q_{crit}$.

This simple model yields the intriguing result that the gas consumption time is directly tied to the overall galactic clock, as would be expected in a marginally stable, Toomre $Q < 0.67$ disk (Elmegreen 1997, Silk 1997, Genzel et al. 2011, Krumholz et al. 2012). The galactic clock is tied to cosmic time, $H(z)^{-1}$, which drives the average size and dynamical timescale of the disk (Mo et al. 1998). Equation 6 assumes a constant angular momentum parameter λ. In reality, angular momentum parameters in galactic disks follow a log-normal distribution with a scatter in $\log \lambda$ of approximately 0.2 (Burkert et al. 2016), such that Equation 6 is valid only for broad averages. Since gas fractions increase upward in the M_*–SFR plane, galaxies above the MS have smaller Q and thus smaller depletion timescales. We conclude that the simple model of a Toomre instability–controlled disk predicts the correct scaling relations, at least at high redshift. It does not predict the zero-point $\varepsilon_T \sim 0.1$ or the star-formation efficiency per dynamical time (ε_{ff}), both of which are likely set on cloud scales (Krumholz & McKee 2005, McKee & Ostriker 2007). The Toomre and global disk instability model (Genzel et al. 2008, Krumholz et al. 2012, Dekel & Krumholz 2013) breaks down in the local Universe, where the average Toomre parameter is significantly above unity ($Q_{gas} \sim 2–8$; Leroy et al. 2008) (**Figure 6a**). In this regime, the velocity dispersion is set by feedback rather than by gravitational instabilities (Ostriker & Shetty 2011, Krumholz et al. 2018, Übler et al. 2019).

t_T: Toomre timescale

t_{dyn}: galactic dynamical time

Toomre stability parameter (Q): <0.67 (1) for a thick (thin) gaseous disk unstable against gravitational collapse; >1 if there is also a stellar disk
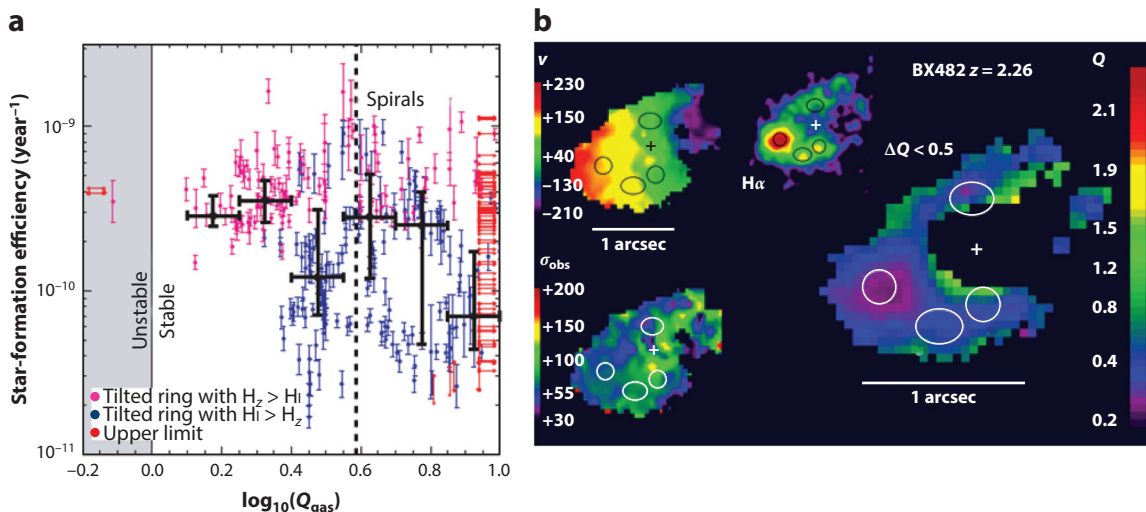
a

b

Figure 6

Variations of the Toomre Q parameter in galactic disks. (*a*) Star-formation efficiency ($1/t_{depl}$) as a function of Q_{gas} in the $z \sim 0$ galaxies of the HERACLES survey. There is no significant dependence of t_{depl} on Q, and all galaxies are in the stable regime of the Q parameter, such that these local star-forming galaxies are likely not controlled by the Toomre global disk instability model. (*b*) Inferred Q_{tot} parameter from the Hα dynamics in the $z \sim 2.26$ disk/ring galaxy BX 482. Molecular column densities are inferred from the scaling relations (or inverted Kennicutt–Schmidt relation). The Toomre Q parameter appears to be below one everywhere in the disk, and the prominent star-formation clump in the east represents a minimum in Q, suggesting that the global instability model is applicable. Panel *a* adapted from Leroy et al. (2008). Panel *b* adapted from Genzel et al. (2011, figure 4).

The question remains regarding whether the Toomre model is also applicable on subgalactic scales. Leroy et al. (2013) have shown that the depletion time does not vary with dynamical time or radius in 30 local SFGs (**Figure 6a**). This lack of correlation is consistent with the fact that $Q > 1$ in these systems (Leroy et al. 2008). Genzel et al. (2011) show that, at high z, $Q < 1$ holds everywhere in several massive star-forming disks on >2-kpc scales, with clear minima at prominent massive star-forming clumps (**Figure 6b**). This finding suggests that the Toomre model may also be applicable in spatially resolved data of high-z SFGs, but extensive, high-resolution mapping at subclump scales will be necessary to draw a definitive conclusion.

4. THE COSMIC EVOLUTION OF COLD GAS RESERVOIRS

4.1. Mass-Integrated Evolution

The previous section discusses the steep increase with z of molecular gas reservoirs in SFGs, derived from pointed observations of massive [$\log(M_*/M_\odot) > 10.0$] systems. The next question is how the mass density of molecular gas per comoving cosmic volume evolves with redshift or time. There are two ways to estimate this quantity. The first is to use the blind technique of summing up the inferred molecular masses for a given redshift bin in the search volume (field area times depth in units of comoving megaparsecs). Several sets of authors have taken this blind approach in GOODS-N (DeCarli et al. 2014; $z = 1.5, 2.5$) with NOEMA, in HUDF (DeCarli et al. 2016, Walter et al. 2016; ASPECS, $z = 1, 2.3$) with ALMA, and in GOODS-N and COSMOS (Riechers et al. 2019; COLDz, $z = 2.5, 6$) with the JVLA. Most recently, Lenkic et al. (2020) analyzed the 110 data cubes of the NOEMA PHIBSS2 pointed CO survey (Tacconi et al. 2018, Freundlich et al. 2019) of $z \sim 0.5$–2.5 MS SFGs to search for additional serendipitous sources
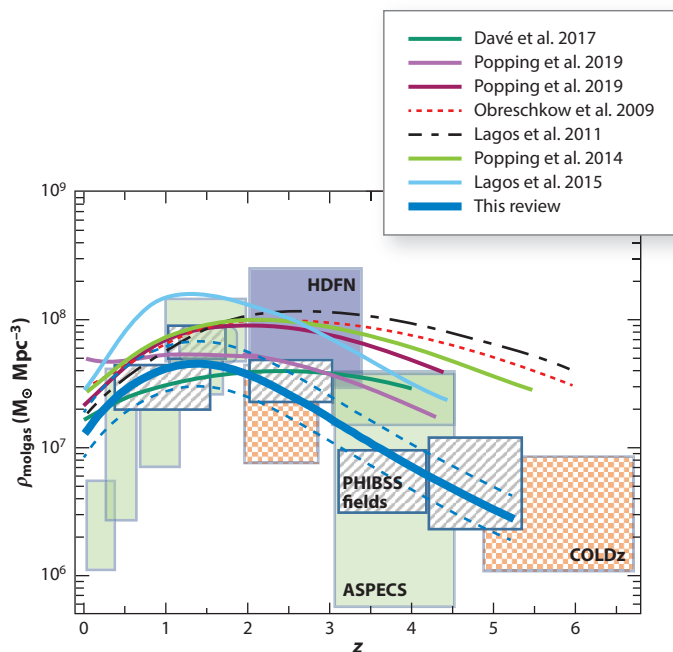
Figure 7

Different observational and theoretical estimates of the cosmic evolution of total molecular mass (H_2 plus helium) density per comoving volume. The different boxes denote estimates at different redshifts with the deep field technique (DeCarli et al. 2014, 2016; Aravena et al. 2016; Walter et al. 2016; Riechers et al. 2019). The gray-shaded boxes show the serendipitous detections of secondary sources in the same data cubes as those from the pointed PHIBSS2@NOEMA survey, which is another way to construct a blind survey (Lenkic et al. 2020). The PHIBSS2 survey covers a larger cosmic volume than the other blind surveys, yielding smaller uncertainties. The thick blue line (with the parallel dashed blue lines denoting the uncertainties) is the star-formation rate volume density of Madau & Dickinson (2014) multiplied by $t_{depl} = 1.6 \times (1 + z)^{-1}$, which describes the consumption time of main sequence galaxies that dominate the star-formation rate (Rodighiero et al. 2011, 2015). For comparison, the various lines denote the results of the semianalytic models and hydrodynamic simulations in the recent literature.

in the NOEMA primary beam field of view. They found 67 candidate sources, ~64% of which have potential optical counterparts. From these equivalently blind data, the authors determined the cosmic molecular mass volume density over redshifts of $z \sim 0.7$ and $z \sim 5$. **Figure 7** shows the compiled results of all these various studies. The molecular mass content per volume increases with increasing redshift, reaches a broad peak at z_{peak}(molgas) $\sim 1.4 \pm 0.3$, and slowly drops toward higher redshift.

A second approach is to use the evolution of the SFR density (Madau & Dickinson 2014) and multiply by the mass-independent depletion time versus redshift scaling of the MS, t_{depl}(MS) $= 1.6 \times (1 + z)^{-1}$, obtained from the pointed technique and discussed above (**Figure 3**). The use of this approach is justified because ~90% of the total cosmic SFR to $z \sim 2$ occurs in MS galaxies (Rodighiero et al. 2011, 2015); outliers in the starburst population above the MS, with 3–10-times-shorter depletion timescales, play only a secondary role in the overall cosmic evolution of the SFR and cold gas mass (**Figure 7**). To within the uncertainties, driven by source number statistics in the deep field technique and the assumption of a single-parameter dependence of the depletion time in the pointed technique, the mass-integrated evolutions of the cosmic molecular gas density

obtained with the two approaches are in very good agreement. The peak redshift of galaxy molecular gas reservoirs is at somewhat lower z than that of the SFR density itself [z_{peak}(SFR) $\sim$ 2].

Essentially all of the semianalytic models shown in **Figure 7** predict that the maximum of the cosmic molecular gas density is at higher redshift ($z \sim$ 2–3). The postprocessing analyses of the hydrodynamic simulations fare better. In particular, the two most recent simulation-based results, from MUFASA (Davé et al. 2017) and IllustrisTNG (Popping et al. 2019), come close to predicting the observed time evolution and the maximum density. **Figure 1b** shows the same curve from the depletion time scaling relation, now in comparison to the evolution of stellar mass from Madau & Dickinson (2014). Both **Figures 1** and **7** show that the molecular gas reservoirs and stellar mass track each other from high z to $z \sim$ 2, and then the molecular gas mass density levels out, followed soon thereafter by that of the stars.

The figures also show the average mass density of atomic hydrogen for comparison. The neutral gas is probed by the 21-cm line in the local Universe and Lyman-α UV absorption spectroscopy in the mid- and high-z Universe (e.g., Keres et al. 2003; Péroux et al. 2005; Zwaan et al. 2005; Rao et al. 2006; Guimarães et al. 2009; Obreschkow & Rawlings 2009a,b; Prochaska & Wolfe 2009; Martin et al. 2010; Braun 2012; Noterdaeme et al. 2012; Popping et al. 2014; Catinella et al. 2018; Rhee et al. 2018). Although no continuous deep field studies are yet available for H I, the atomic hydrogen distribution is quite flat [$\rho_{H I}$ M$_\odot \sim 5.6 \times 10^7 \times (1+z)^{0.5}$ Mpc^{-3}] and is decoupled from the rapid evolution of molecular or stellar mass and SFR. A possible concern is that the local galaxy H I measurements measure the gas within galaxies, while the absorption line measurements at higher redshifts probe gas in the galaxies, as well as in the CGM. We refer the reader to the article by Péroux & Howk (2020) in this volume for more details.

4.2. Molecular Gas Mass and Star-Formation Rate Density

Here we discuss the evolution of mass and SFR distribution functions. **Figure 8** summarizes the current observational and theoretical knowledge in molecular mass and SFR as a function of gas mass, in two redshift slices, $z = 0$ and $z = 2$. **Figure 8a,c** shows molecular mass functions (per logarithmic mass interval) from the metallicity-based recipes of Popping et al. (2014), based on the Gnedin (2000) and Kravtsov et al. (2004) treatment of reionization, baryonic collapse, and H$_2$ formation. The Popping et al. (2014) and Lagos et al. (2015) models predict a broad mass function at all three redshifts, with a peak at $\sim$7–10 $\times 10^9$ M$_\odot$, and a broad shoulder toward lower masses, so that the median mass is less than half the peak mass. We compare these predictions to the observed $z = 2.2$ mass functions, from a combination of ASPECs (DeCarli et al. 2016), COLDz (Riechers et al. 2019), and PHIBSS2 deep field data at that redshift (Lenkic et al. 2020); *Herschel* far-IR continuum data (Vallini et al. 2016); and conversion of the Madau & Dickinson (2014) SFR data to molecular masses with the depletion time scalings. The data and models agree reasonably well at $z = 0$, possibly in part because of the calibration of semianalytic model parameters on the $z = 0$ data.

At $z = 1$–2, there is significant tension between the observed and theoretically predicted molecular gas fractions and mass-integrated molecular gas volume densities at the high-mass end (**Figures 8b,d** and **9a**), which has been noted in the discussions of most recent observational and theoretical papers. Independently of whether the molecular data originates from pointed observations or from deep fields, the empirical results exhibit a high-mass shoulder or bump that is not present in any of the models and simulations. The same is true for the high-mass tail of the SFR distributions at high z. The most recent MUFASA simulations (Davé et al. 2017) and IllustrisTNG-based research (Popping et al. 2019) do a better job (**Figure 8a,c**). Given the excellent agreement between the pointed and deep field techniques, and between the different
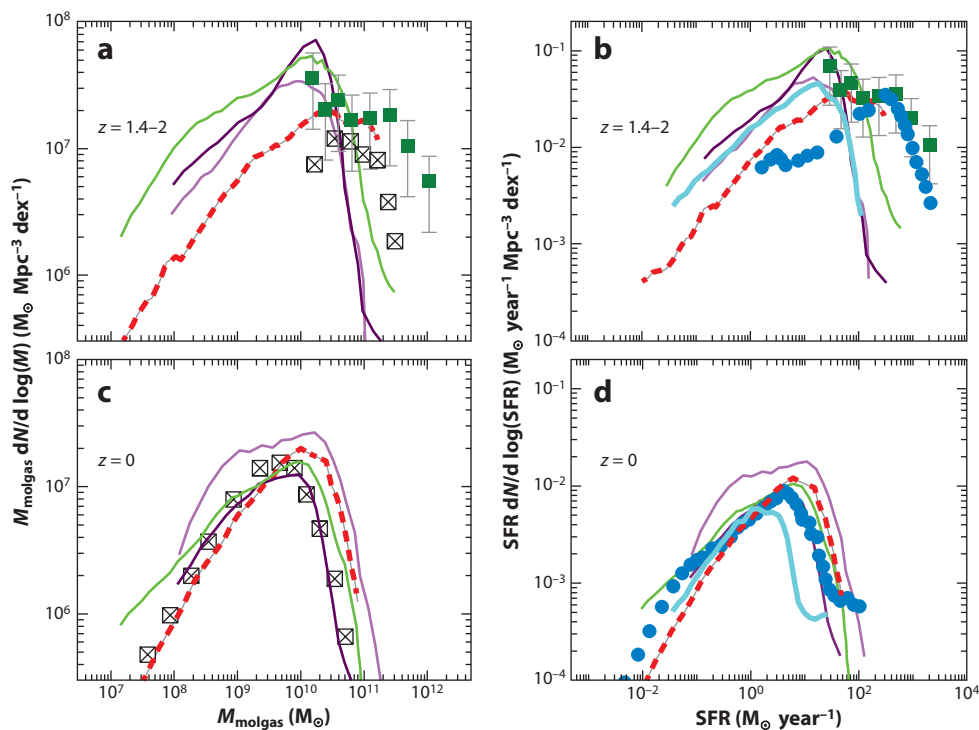
Figure 8

Predicted and observed mass (*a,c*) and SFR (*b,d*) distribution functions (per comoving volume and per logarithmic mass/SFR interval) for $z = 0$ (*c,d*) and $z = 2$ (*a,b*). (*c*) The green and thick dotted red curves denote the molecular mass per logarithmic mass interval per cosmic comoving volume [$M_{mol} \times$ dN/d log (M_{molgas})] at $z = 0$ from the SAMs of Popping et al. (2014) and the MUFASA simulation of Davé et al. (2017), respectively. The continuous purple and light purple lines are the Santa Cruz SAMs and the IllustrisTNG simulations results from Popping et al. (2019), respectively. The crossed black rectangles are derived from *Herschel* observations and turning the far-IR luminosity function into a molecular mass distribution function (Vallini et al. 2016). (*a*) Same as in panel *c*, but for $z = 1.4$–2. The filled green squares denote the observed mass functions from current deep field observations at $z \sim 2$–2.5 (Decarli et al. 2014, 2016, 2019; Walter et al. 2016; Lenkic et al. 2020, their figure 13; Riechers et al. 2019). (*d*) $z = 0$ SFR distributions [SFR dN/d log(M_{molgas})] from the same theoretical research as in panels *a* and *c*, as well as from the postprocessing of the EAGLE cosmological simulation (Schaye et al. 2015) by Lagos et al. (2015) (*cyan*). The blue circles denote estimates obtained from combining the UV- and far-IR luminosity functions of Madau & Dickinson (2014) and multiplying the result by SFR/$t_{depl} = 1.6 \times (1 + z)^{-1}$, where we assume that a luminosity of 10^{10} $L_\odot$ corresponds to an SFR of 1 $M_\odot$ year^{-1} (Chabrier IMF). (*b*) The same as in panel *d*, but for $z = 1.4$–2. The green squares denote the mass density in panel *a* (obtained from all deep field observations) divided by $t_{depl} = 1.6 \times (1 + z)^{-1}$ to turn the mass functions into SFR functions. Abbreviations: IMF, initial mass function; SAM, semianalytic model; SFR, star-formation rate.

molecular mass estimators, it is unlikely that the tension lies with uncertainties in the CO–H$_2$ conversion factor, as proposed by Popping et al. (2019). The only obvious problem in the data might be a zero-point issue. The zero points from Scoville et al. (2017) would make things even worse (**Figure 9***a*), and the relatively good agreement between observations and theory at $z = 0$ (**Figures 8** and **9**) would indicate a redshift-dependent zero-point problem. This is in principle possible, since all three techniques transfer $z = 0$ calibrations to higher z. If the tension between predicted and observed molecular masses is the result of assumptions in the theoretical models,
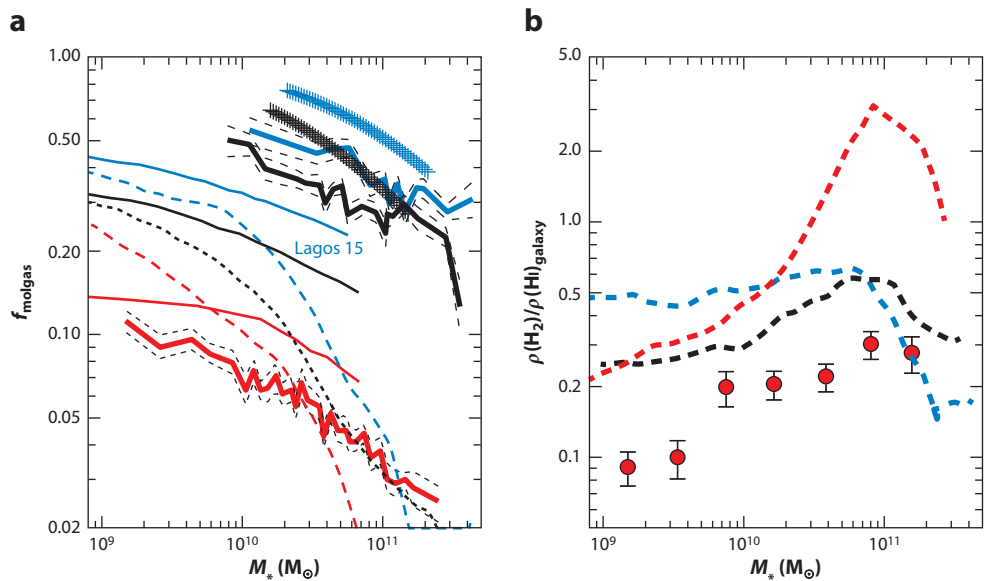
Figure 9

Estimates of fractions of molecular gas to stellar plus molecular mass and of molecular mass to atomic gas, as
a function of stellar mass and redshift. (*a*) Red, black, and blue lines represent molecular gas fractions
$\{f_{\mathrm{molgas}} = (M_{\mathrm{molgas}}/M_*)/[1 + (M_{\mathrm{molgas}}/M_*)]\}$ as a function of stellar mass at $z = 0$, 1, and 2, respectively.
Solid lines represent the semianalytic models of Popping et al. (2014), dotted lines represent the MUFASA
simulations of Davé et al. (2017), and Lagos 15 refers to the $z = 2$ results from processing the EAGLE
simulations. The data from our master set are shown as thick solid lines, with black dashed lines marking the
$\pm 1\sigma$ scatter. Black and blue crosses represent the Scoville et al. (2017) scaling relations at $z = 1$ and 2,
respectively. To first order, the Scoville et al. (2017) gas fractions are higher than the results from this review
and from Tacconi et al. (2018) because of the 50%-larger CO conversion factor. (*b*) Thick dashed curves
represent the intragalaxy H_2-to-H_I ratios from the MUFASA simulations in the three redshift bins, as in
panel *a*. The observed ratios are represented by a thick red dots on gray circles (from Catinella et al. 2018).

a possible solution might be the efficiency and mass dependence of the stellar feedback and the
recycling of related wind gas (Oppenheimer et al. 2010) (see the sidebar titled Recycling).

   All theoretical studies predict most of the molecular gas to be associated with low-mass systems
(**Figures 8** and **9**), yet neither the pointed nor the deep field approach has been able to assemble
statistically meaningful results for $<10^{10}$ $M_\odot$ galaxies at high z or for $<10^9$ $M_\odot$ galaxies at $z = 0$.
This failure has been discussed in detail in the literature (see Section 2.1.2 for references) and is
plausibly closely connected to the photodissociation of CO (dark gas) and low dust-to-gas ratios
in low-metallicity systems, making low-mass systems hard to detect.

4.3. The Gas Regulator Model

Many of the basic results discussed in this review can be understood in a simple, and observation-
ally testable, analytical framework by considering the flow of gas into galaxies, conversion into
stars by in situ star formation, and ejection of gas out of galaxies by stellar or AGN feedback. This
so-called bathtub (Bouché et al. 2010, Davé et al. 2012, Dekel & Mandelker 2014, Somerville
& Davé 2015) or gas regulator (Lilly et al. 2013, Peng & Maiolino 2014) model starts with the

RECYCLING

For momentum-driven winds, the outflow mass loading factor, $\eta = \dot{M}_{out,wind}/\text{SFR}$, as well as the ratio of outflow to circular velocity, should correlate with galaxy mass M as $\eta \sim M^{-1/3}$ (Murray et al. 2005, Oppenheimer et al. 2010) or with $\eta \sim M^{-2/3}$ for energy-driven winds (Faucher-Giguère & Quataert 2012). Small galaxies (at high z) would form inefficiently and lose much of the incoming gas to the CGM, in agreement with abundance-matching results (e.g., Behroozi et al. 2010, Moster et al. 2013). If the outflow velocities are not sufficient to fully expel the gas from the halo, some could return as fountains at later times, when the galaxy is more massive, resulting in accretion rates and gas fractions above $\eta = $ constant models (Davé et al. 2011a, Dekel & Mandelker 2014). The recycling time t_{rec} scales inversely with mass, such that for galaxies above $\log(M_*/M_\odot) \geq 10.5$ the recycling time is $\sim$0.5–1 Gyr (Oppenheimer et al. 2010), so that gas ejected at $z \sim 2$ returns at $z \sim 1.5$ and could substantially increase gas accretion rates, SFRs, and gas reservoir masses. Recycling processes are probably well captured only in hydrodynamic simulations with strong winds, which do well on the peak reservoir redshift in **Figures 1** and **7**, and much better for the high-mass gas fractions.

continuity equation for gaseous and stellar matter:

$$\dot{\Phi} = (1 - R + \eta) \times \text{SFR} + \dot{M}_{molgas}. \qquad 7.$$

The left-hand side of this equation is the accretion rate of gas into the galaxy, and M_{molgas} and $\dot{M}_{molgas}$ are the mass and the change in mass of the molecular gas in the galaxy, respectively. R is the return fraction of gas back into the galaxy by massive stars (0.4 for Chabrier IMF), and η is the mass loading of stellar feedback, as defined in Section 4.2. The last term on the right-hand side is the time derivative of the galactic molecular gas reservoir (i.e., the level of the reservoir). Simulations show that the baryonic accretion rate into the galaxy, $\dot{\Phi}_{gal,baryon}$, and the dark matter accretion rate into the halo, $\dot{\Phi}_{h,DM}$, can be written as (Genel et al. 2008, Neistein & Dekel 2008)

$$\dot{\Phi}_{gal,baryon} = f_{gh} \times f_{baryon} \times \dot{\Phi}_{h,DM} = 6.3 \times f_{gh} \times \left(\frac{f_{baryon}}{0.18} \right)$$

$$\times \left(\frac{M_h}{10^{12} M_\odot} \right)^{1.15} \times (1 + z)^{2.35} M_\odot \text{ year}^{-1}, \qquad 8.$$

for a halo mass M_h at z, cosmic baryon–to–dark matter fraction f_{baryon}, and transport efficiency factor from halo to galaxy f_{gh}. Recalling that $M_{molgas} = \text{SFR} \times t_{depl}$ and $\mu = M_{molgas}/M_*$, we can reformulate Equation 8 as follows:

$$\dot{\Phi}_{gal,baryon} = \left[(1 - R) \times (1 + \mu_{molgas}) + \eta + t_{depl} \frac{d \ln \mu_{molgas}}{dt} \right] \times \text{SFR}, \quad \text{and}$$

$$\dot{M}_{molgas} = \mu_{molgas}(1 - R) \times \text{SFR} + M_* \frac{d\mu_{molgas}}{dt} = \left[\tau_{depl} \frac{d \ln \mu_{molgas}}{dt} + \mu_{molgas} \times (1 - R) \right] \times \text{SFR}.$$
$$9.$$

By taking the Lilly et al. (2013) formulation of Equation 1, one can easily calculate the gas accretion rate density and gas reservoir change required from the observed SFR (Madau & Dickinson 2014) volume density and the properties of the gas reservoir (Section 3) and compare them with the expected accretion rate from the simple, dark matter–based estimator above. **Figure 1a** shows the results for the simple (but not realistic) ansatz $\eta = $ constant.

t_{rec}: recycling time, which is 0.5–1 Gyr, for gas ejected by (stellar) feedback to return back to the galaxy, in effect increasing the gas accretion rate from the CGM above the level of cosmic accretion, especially at $z \sim 0.5$–1.5

η: the outflow mass loading factor, $\eta = \dot{M}_{out,wind}/\text{SFR}$

Recall that the maximum gas accretion rate is an upper limit for the baryonic accretion due to the cosmic growth of the halo. For comparison, **Figure 1a** also shows the accretion rates obtained with the above estimate from the gas regulator, for outflow mass loading $\eta = 2$ and $\eta = 1$, respectively. To first order, the two rates are comparable between $z = 0$ and $z = 5$. At the peak of the cosmic galaxy/star-formation activity ($z \sim 2$), the cosmic accretion upper limit is below the outflow mass loading $\eta = 1$, certainly for the large mass loading factor of $\eta = 2$. Again, this finding suggests qualitatively that recycling of the wind-ejected matter may be an important aspect of the gas evolution (Oppenheimer et al. 2010; Davé et al. 2011a,b, 2012).

Figure 1a shows the change in the level of the gas regulator. In the ideal regulator, the gas reservoir level of the bathtub does not change, and the galaxy SFR is tied only to the baryonic accretion rate from the halo. At high z, the gas accretion time, $t_{acc} = M_{molgas}/(dM_{molgas}/dt)$ is shorter than the depletion time, such that the level of the gas reservoir rises, and the galaxy is fed gas faster than it can convert it to stars (Lilly et al. 2013). Starting at the $z \sim 2$ peak of the SFR, this situation reverses and the regulator becomes more ideal, although the recycling fountains may keep the molecular gas reservoirs high at late times, thereby pushing the time of maximum molecular mass beyond that of the peak of star formation. Overall, the simple gas regulator model is remarkably effective in describing the properties and evolution of the gas and SFRs in galaxies.

Finally, the growth of massive black holes (**Figure 1a**) follows that of the stars closely, as has been pointed out many times (e.g., Madau & Dickinson 2014). This observation suggests that coevolution between the stellar and black components holds on average, with large fluctuations in time due to the much more time-variable activity and evolution of the black hole component (Mullaney et al. 2012, Hickox et al. 2014, Delvecchio et al. 2015).

4.4. Disk Instabilities, Radial Transport, and Bulge Formation

Galaxy-integrated models of equilibrium growth yield only a first-order picture. Spatially resolved semianalytic models and hydrodynamic simulations provide detailed insight into the circumgalactic and subgalactic workings of the regulator (Forbes et al. 2012, 2014; Genel et al. 2014; Hopkins et al. 2014; Lagos et al. 2015; Zolotov et al. 2015; Anglés-Alcázar et al. 2017; Bower et al. 2017; Davé et al. 2017; Krumholz et al. 2018; Nelson et al. 2019; Pillepich et al. 2019). Counterrotating CGM streams, mergers, and global Toomre-scale instabilities in gas-rich disks create gravitational torques and rapid angular momentum redistribution at high z. As a result, gas (and stars) is transported radially from the outer disk to a growing central bulge on the dynamical friction or viscous timescale: $t_{dv} \sim t_{dyn}(R_e) \times (v_c/\sigma_0)^2 \sim$ a few $\times 10^8$ years at $z \sim 2$ (Noguchi 1999; Immeli et al. 2004; Genzel et al. 2008; Dekel et al. 2009b; Forbes et al. 2012, 2014; Dekel & Krumholz 2013; Zolotov et al. 2015; Rathaus & Sternberg 2016). Likewise, the baryon cycle and these transport processes determine the metallicity evolution of galaxies and plausibly establish the exponential form of the stellar distribution (Davé et al. 2011b; Forbes et al. 2012, 2014; Lilly et al. 2013; Rathaus & Sternberg 2016). Observational evidence for these fast transport processes and the subsequent compaction (Zolotov et al. 2015) has come from studies of high-z gas kinematics (e.g., Genzel et al. 2008) and the occurrence of compact blue optical nuggets (Barro et al. 2013), or compact nuclear submillimeter dust concentrations (Barro et al. 2016, Tadaki et al. 2017). These systems might be the precursors of the population of compact high-z passive galaxies (Daddi et al. 2005, Trujillo et al. 2006, van Dokkum et al. 2008, Genzel et al. 2014a, Tacchella et al. 2015). Gas-rich, globally Toomre unstable, or marginally stable [$Q \leq Q_{crit} \sim O(1)$; see Section 1.1] galaxies are turbulent and geometrically thick: $(\sigma_0/v_c) \sim (h_z/R_d) \sim Q \times f_{gas}/a$, with $a \sim 1.4$–1.7 (Genzel et al. 2008, Dekel et al. 2009b). For typical gas fractions at $z \sim 2$ and $f_{gas} \sim 0.45$, the Toomre instability model predicts $(\sigma_0/v_c)_{z=2} \sim (h_z/R_d)_{z=2} \sim 0.25$–0.3. This value is in excellent agreement with those from observations, including the continuous decrease of σ_0 with redshift (see Sections 1.4

t_{dv}: radial transport time due to dynamical friction, torques, and viscosity

and 3.5) (Förster Schreiber et al. 2006, 2009; Kassin et al. 2012; Wisnioski et al. 2015; Übler et al. 2019). It is tempting to speculate that the highly turbulent, gas-rich phase of disk galaxies can (at least in part) be identified with the thick disk in the modern Milky Way and other spiral galaxies (Gilmore et al. 1989, Bournaud et al. 2009). In the simulations, galaxies move up and down the MS on typical timescales of approximately $0.4\,H(z)^{-1}$ (Tacchella et al. 2016), as a result of these perturbations and of fluctuations in the accretion rates driven by the geometry and angular momenta of the cosmic streams feeding the galaxies.

4.5. The Balance of H_2 to H I Cold Gas Components in Galaxies

In Section 3, we discuss the rapid increase of molecular gas fractions and molecular gas volume density with increasing look-back time, leveling off at $t_{lb} \sim 10$–12 Gyr ($z \sim 2$–3), and matching the same behavior of SFRs and expected accretion rates from the halo (**Figure 1**). Between $z = 0$ and $z = 2$, the molecular hydrogen content of the Universe more than quadruples, and gas-to-stellar fractions increase by an order of magnitude. Before $z \sim 2$, the growth of molecular gas and of stellar mass density tracked each other. At and after the $z \sim 2$ peak, gas reservoirs and fractions began to drop and massive SFGs stopped growing and transitioned to the passive galaxy sequence. **Figure 1b** shows the atomic hydrogen content of galaxies (and their CGMs), as estimated from 21 H I emission observations at $z < 0.4$ and from Lyman-α observations in absorption against stars and distant AGN. The cosmic atomic hydrogen density per comoving volume, integrated over all galaxy masses, increased by only 50% between $z = 0$ and $z = 2$. Since at least a fraction of the hydrogen at high z inferred from Lyman-α plausibly resides in the CGM, the atomic hydrogen content in the central galaxies may increase even less. Yet the cold ISM in SFGs of all masses, and especially at low redshifts and low masses, is predominantly in the form of atomic hydrogen (**Figure 9b**) (Young & Scoville 1991, Saintonge et al. 2011a, Catinella et al. 2018). Catinella et al. (2018) find $\log(M_2/M_{H I}) = 0.265 \times [\log(M_*) - 10.7] - 0.62$. While the central star-forming disks are dominated by molecular hydrogen, the outer disks are mostly atomic (Young & Scoville 1991, Leroy et al. 2009, Saintonge et al. 2016). These observational findings are broadly captured by theoretical research in both semianalytic models (Lagos et al. 2011; Forbes et al. 2012, 2014; Popping et al. 2014) and simulations (e.g., Lagos et al. 2015, Davé et al. 2017).

4.6. What Drives the Ratio of H_2 to H I?

Hydrogen gas in the ISM of galaxies is present in atomic (H I) form in diffuse clouds with low visual extinctions, and in molecular (H_2) form in dense optically thick regions (such as in GMCs) that are well shielded against molecular photodissociation. Full conversion of H I to H_2 is necessary for the complete incorporation of gas-phase carbon into CO molecules (Jansen et al. 1995, Sternberg & Dalgarno 1995). However, this is not a sufficient condition, because CO is more susceptible to photodissociation than is H_2, especially at low metallicities (Wolfire et al. 2010, Nordon & Sternberg 2016; see Section 2.1.2).

In the diffuse medium, H I can exist in two phases: (*a*) the warm $\sim 8 \times 10^3$ K neutral medium (WNM), in which cooling is dominated by a combination of Lyman-α emission and, depending on metallicity, electron recombination onto small grains and polycyclic aromatic hydrocarbons and (*b*) the cool ~ 100 K neutral medium (CNM), where the energy losses are via metal fine-structure line emissions, especially the C^+ 158-μm line (Field et al. 1969, Draine 1978, Wolfire et al. 2003, Bialy & Sternberg 2019). Heating occurs by far-UV absorption followed by ejection of electrons from dust grains (photoelectric effect), cosmic-ray ionization of the hydrogen atoms, and dissipation of turbulence. In general, the H I is pure WNM at sufficiently low volume densities, where cooling is inefficient, and pure CNM at high densities, where the collision rates are

rapid. Depending on the heating rates and the gas-phase metallicities and dust abundances, the two phases can coexist for a narrow range of thermal pressures. CNM condensations are then embedded within an enveloping WNM, observable as narrow 21-cm CNM emission or absorption features across broad WNM emission profiles (e.g., Dickey & Brinks 1993, Heiles & Troland 2003, Warren et al. 2012, Stanimirović et al. 2014). The H I gas in galaxies may often be self-regulated to a multiphased WNM/CNM state by a feedback loop (Krumholz et al. 2009, Ostriker et al. 2010; see also Schaye 2004). For a given galaxy disk pressure, as set by, for example, the overlying weight of the ISM, and under the assumption that star formation requires the presence of CNM, the SFR will adjust such that the H I becomes multiphased. If the SFR is too large, the elevated heating rates will drive the gas to WNM, thereby reducing the SFR and heating rates and enabling conversion back to CNM.

In dense, optically thick clouds, the atomic-to-molecular (H I-to-H$_2$) transition is controlled by the balance between H$_2$ formation on the surfaces of dust grains and H$_2$ destruction by far-UV photodissociation. With increasing cloud depth, the H$_2$ photodissociation rates are reduced by a combination of dust opacity as well as H$_2$ absorption line opacity in the Lyman–Werner molecular band systems through which photodissociation occurs. Both the H$_2$-formation efficiency and the dust absorption opacity depend on the dust-to-gas ratio or the metallicity of the gas. The H$_2$-formation rate is proportional to the gas density, and for a sufficiently weak radiation field, the H I-to-H$_2$ conversion is controlled by H$_2$ absorption line self-shielding. In this weak field regime the conversion point occurs at a very low dust optical depth, and most of the photodissociated H I is present (in trace amounts) inside the molecular zones. For sufficiently intense radiation fields, the photodissociation rate is attenuated by the dust opacity associated with large H I column densities. In this strong field regime, most of the H I is present as a fully photodissociated surface layer surrounding an internal molecular zone. Thus, the primary parameters controlling the H I-to-H$_2$ transition are the gas density (or pressure), the intensity of the free-space far-UV field, and the metallicity, which determines the H$_2$-formation rate coefficient and dust absorption opacity. In the fully shielded molecular zones, heating is inefficient and the gas becomes cold (<50 K).

Cloud structures, in terms of both density inhomogeneities and velocity distributions (e.g., as imprinted by turbulent motions), are a major complication because of the effects on the shielding and radiative transfer properties of the gas. Treatments of the H I-to-H$_2$ conversion in hydrodynamic simulations (cosmological or zoom-in) and in semianalytic models therefore require the adoption of (possibly quite crude) subgrid recipes, usually based on simple analytic single-cloud formulae (Sternberg 1988, Elmegreen 1993, Blitz & Rosolowsky 2006, Krumholz et al. 2008, McKee & Krumholz 2010, Gnedin & Kravtsov 2011, Sternberg et al. 2014). Such recipes have been used in computations in which star formation is assumed to require the presence of H$_2$ (Fu et al. 2010; Christensen et al. 2012; Kuhlen et al. 2012; Popping et al. 2014, 2015; Thompson et al. 2014; Davé et al. 2016; Xie et al. 2017), or simply for partitioning the cold gas between H I and H$_2$ (Obreschkow et al. 2009; Lagos et al. 2011, 2015; Bekki 2013; Marinacci et al. 2017; Diemer et al. 2018). Simulations have also been carried out in which the (nonequilibrium) H$_2$-formation/destruction chemistry is computed on the fly using subgrid prescriptions for the photodissociating radiation fields and cold gas densities (Robertson & Kravtsov 2008; Tomassetti et al. 2015; Hu et al. 2016; Lupi et al. 2018; Nickerson et al. 2018, 2019).

A simple expression for the H$_2$ gas fraction, f_{H_2}, in optically thick, uniform-density, 1D (plane-parallel or spherical) clouds with a total hydrogen (atomic plus molecular) column density N (cm^{-2}) is (Sternberg et al. 2014)

$$f_{H_2} = 1 - \frac{N_{HI}}{N} = 1 - \frac{1.6\sigma_g^{-1} \times \ln(\alpha_{df}G/3.2 + 1)}{N},$$ 10.

where σ_g is the metallicity-dependent dust absorption cross section per hydrogen nucleus and N_{HI} is the total HI column density that is produced by photodissociation for two-sided illumination of a plane-parallel slab or, equivalently, isotropic irradiation of a sphere (and neglecting cosmic-ray destruction of the H_2). Equation 10 is for optically thick clouds, for which $N > N_{\mathrm{HI}}$ by definition. In this expression, $\alpha_{\mathrm{df}} = D/R'n$ is the ratio of the free-space H_2 dissociation rate, D, to the molecular formation rate, $R'n$, where R' is the grain-surface formation rate coefficient of H_2 and n is the total (atomic plus molecular) gas density. G is a metallicity-dependent cloud-averaged H_2 self-shielding factor. The product, $\alpha_{\mathrm{df}}G$, is the primary dimensionless parameter in the problem, given by

$$\alpha_{\mathrm{df}}G = 1.54 \times \left(\frac{\sigma_g}{1.9 \times 10^{-21}\,\mathrm{cm}^{-2}}\right) \times \left(\frac{F_{\mathrm{UV}}}{2 \times 10^7\,\mathrm{cm}^{-2}\,\mathrm{s}^{-1}}\right)$$
$$\times \left(\frac{R'}{3 \times 10^{-17}\,\mathrm{cm}^3\,\mathrm{s}^{-1}}\right)^{-1} \times \left(\frac{n}{10^2\,\mathrm{cm}^{-3}}\right)^{-1} \times [1 + (2.64Z')^{0.5}]^{-1}. \qquad 11.$$

In this expression, F_{UV} is the flux of far-UV photons in the Lyman–Werner bands and Z' is the metallicity in units of solar metallicity. The above equation is quite general and provides insight into the behavior of the H_2 gas fraction in terms of the above parameters. For $\alpha_{\mathrm{df}}G < 1$, H_2 self-shielding controls the atomic-to-molecular transition. For $\alpha_{\mathrm{df}}G > 1$, the transition is governed by dust absorption of the radiation. For any value of $\alpha_{\mathrm{df}}G$, N_{HI} is inversely proportional to σ_g. This means that the atomic column at the surface of the cloud is larger for smaller metallicities, and the total cloud column $N = 2N_{\mathrm{HI}}$ required for a given H_2 mass fraction is correspondingly larger. If the self-regulation ansatz for multiphased HI gas is assumed (Krumholz et al. 2009), then $\alpha_{\mathrm{df}}G \sim 2$ for the CNM, or $N_{\mathrm{HI}} = 0.7/\sigma_g$. With this assumption, $f_{\mathrm{H_2}} = 0.5$ occurs for clouds with $N = 1.4/\sigma_g$, corresponding to a mass density of $N_{\mathrm{crit}} = 12/Z'\,\mathrm{M}_\odot\,\mathrm{pc}^{-2}$, for σ_g scaling linearly with metallicity Z', in units of solar metallicity.

Another estimate of this critical column density comes from observations of the HI and H_2 gas content of nearby galaxies. Blitz & Rosolowsky (2006) find that the ratio of H_2 to HI varies as $P_e^{0.9}$, where P_e is the pressure. Since $P_e \propto \Sigma_{\mathrm{gas}}^2$, the authors find $H_2/\mathrm{HI} \sim (\Sigma_\mathrm{H}/45\,\mathrm{M}_\odot\,\mathrm{pc}^{-2})^{1.8}$. The critical column density at which $H_2/\mathrm{HI} = 1$ (i.e., $f_{\mathrm{H_2}} = 0.5$) is in rough agreement with the photodissociation argument. This critical column density is also in good agreement with a kink in the KS plane of $\Sigma_{\mathrm{gas}} - \Sigma_{\mathrm{SFR}}$, below which the slope of the relation becomes much steeper than $N_{\mathrm{KS}} = 1$–1.4 (Wong & Blitz 2002, Bigiel et al. 2008, Kennicutt & Evans 2012).

The observed evolution of the cosmic molecular hydrogen–to–atomic hydrogen ratio is matched quite well by theoretical research, especially the most recent simulations (**Figure 1b**) (Davé et al. 2017). This research shows that the above-described modeling techniques probably do a satisfactory job for the global evolution of the gas reservoirs.

5. STARBURST GALAXIES

So far, our review has focused on MS galaxies that grow in quasi-equilibrium at the average gas accretion rate (Equation 8). In this case, the growth time of the galaxy is directly proportional to the growth time of the dark matter halo, $t_{\mathrm{DM}} = M_{\mathrm{DM}}/\dot{M}_{\mathrm{DM}} \approx 2.1 \times [(1+z)/3]^{-2.3}$ Gyr, for a halo mass of $10^{12}\,\mathrm{M}_\odot$. The mass dependence of t_{DM} is very shallow: $t_{\mathrm{DM}} \propto M_{\mathrm{DM}}^{-0.15}$. The growth time of the stellar component is $t_* = M_*/[\mathrm{SFR} \times (1-R)] = 0.53 \times [(1+z)/3]^\gamma$ Gyr, where $\gamma = -3$ for $z = 0$–2 and $\gamma = -1.67$ for $z > 2$ (Lilly et al. 2013). Note that the stellar component grows faster by a factor of approximately two ($z \sim 0$) to four ($z \sim 2$) than the dark matter halo because of the effects of feedback, reducing the numerator at early times. Since the mass loading

t_{DM}, t_{acc}, and t_*:
growth timescales of the dark matter halo, molecular gas mass, and stellar mass, respectively

for momentum-driven stellar feedback is expected to scale as $\eta \sim v_c^{-1-2}$ (Davé et al. 2012), smaller galaxies have a shallower potential and more powerful winds.

A 10^{12} M$_\odot$ halo will experience a binary major merger (<3:1 mass ratio) every $t_{\text{major merger}} \sim$ 4.4 Gyr $\times [(1 + z)/3]^{-2.1}$ (Neistein & Dekel 2008; Fakhouri & Ma 2009; Genel et al. 2009, 2010). This is comparable to the timescale when two nodes of the cosmic web merge and, therefore, the angular momentum of the gas coming into the galaxy changes drastically (A. Dekel, personal communication). Once that happens, the two galaxies will experience strong gravitational torques that drive gas inward, compress it in the central regions, and trigger an elevated starburst activity (Mihos & Hernquist 1996). Minor mergers with mass ratios of 3:1 to 10:1 are several times more frequent but naturally have a lower efficacy in triggering bursts of elevated star formation. Interaction-driven starbursts last for typically a few dynamical times of the merger, $\sim 10^8$ years $\ll$ t_{depl}(MS). The phenomenon of interaction-driven starburst activity was initially discovered in nearby dusty galaxies, such as M82 and NGC 253 (e.g., Rieke et al. 1980, 1993; Heckman et al. 1998). Sanders et al. (1988), Rowan-Robinson & Crawford (1989), and other researchers have found extreme versions of dusty, IR-bright starbursts in the IRAS survey: ULIRGs (e.g., Sanders & Mirabel 1996). ULIRGs form stars at 100–300 M$_\odot$ year^{-1}, which is approximately two orders of magnitude above the $z = 0$ MS at their stellar mass of a few $\times 10^{10}$ M$_\odot$. ULIRGs are invariably mid- to late-stage major mergers of moderately massive and gas-rich disks, with star formation and AGN contributing to the total luminosities (Genzel et al. 1998).

A possibly analogous, highly obscured star-forming population at high z (SMGs) was discovered through submillimeter observations with the SCUBA submillimeter bolometer (e.g., Smail et al. 1997, Blain et al. 2003). SMGs are often described as scaled-up, high-z versions of ULIRGs, with SFRs of 300–2,000 M$_\odot$ year^{-1}. Many SMGs are indeed compact, merger-driven starbursts much above the $z \sim 1$–3 MS (e.g., Tacconi et al. 2006, 2008; Engel et al. 2010; Bothwell et al. 2013; Hodge et al. 2013, 2016; Casey et al. 2014; Wiklind et al. 2014). Others are very massive MS galaxies at the tip of the mass–SFR relation at $z \sim 2$ (Michałowski et al. 2012). The widest *Herschel* survey, ATLAS, uncovered a more extreme, rare population of hyperluminous galaxies with $L_{\text{IR}} > 10^{13}$ L$_\odot$ (Eales et al. 2010). Many of these are extremely luminous as a result of amplification through strong gravitational lensing (e.g., Frayer et al. 2011, Valtchanov et al. 2011).

ULIRGs and SMGs are more than 100 times as rare as the overall $\log(M_*/M_\odot) > 10$ MS population at the same redshift. Rodighiero et al. (2011, 2015) have shown conclusively that these starbursts make up 6–15% of the cosmic SFR density at $z = 0$–2. The star formation and ISM physics in these objects are extreme and very different from those of typical MS systems (e.g., Downes & Eckart 2007, Hodge et al. 2016, Scoville et al. 2017), and we have included extreme objects in assembling scaling relations as a function of MS offset (see Section 3) (**Table 1**). The scope of this review does not allow us to discuss these interesting outlier objects in more detail, however, and there are recent comprehensive reviews on this topic in the literature (e.g., Casey et al. 2014, Wiklind et al. 2014).

6. SUMMARY AND CONCLUDING REMARKS

6.1. Baryonic Accretion as the Main Driver of Cosmic Star/Galaxy Formation

We have emphasized the wealth and increasing robustness of new observations of the cosmic evolution of molecular (and atomic gas) in galaxies obtained during the last decade. These new observations motivate a model framework for the baryon cycle, star formation, and the cosmic growth of galaxies. In the basic picture, most galaxy evolution at and since the maximum of cosmic star formation 10 Gyr ago took place in rotationally supported disks, which grew mostly through semicontinuous baryonic gas accretion (and minor mergers) from the cosmic web and

internal, local star formation in dense, dusty molecular gas. Throughout this epoch, the galaxy-formation efficiency was ∼10–20% (of the cosmic baryons) within a halo mass range from 10^{11} to $10^{12.5}$ M$_\odot$ but was drastically reduced outside this range (Bouché et al. 2010, Davé et al. 2012, Behroozi et al. 2013). The low formation efficiency of galaxies at the low-mass end is likely caused by stellar feedback and photoionization at high z. At the high-mass end, at and above the Schechter mass (halo masses > 10^{12} M$_\odot$), the low efficiency is probably due to a combination of inefficient gas cooling in the halo and AGN feedback (Rees & Ostriker 1977, Croton et al. 2006, Dekel & Birnboim 2006, Bouché et al. 2010, Nelson et al. 2019). The prominent maximum in cosmic SFR and galaxy-formation rate ∼10 Gyr ago ($z \sim 1$–3; Lilly et al. 1996, Madau et al. 1996, Steidel et al. 1996, Madau & Dickinson 2014) was thus due primarily to higher gas accretion rates and secondarily to more efficient star formation in globally unstable, gas-rich systems.

6.2. The Drivers of the Cosmic Baryon Cycle

Many of the galaxy-integrated stellar, star-formation, and gas properties, and their mutual scaling relations, are captured in various versions of a simple equilibrium gas regulator model, which exploits the mass continuity rate equation in either a galaxy-integrated or spatially resolved fashion (Bouché et al. 2010; Davé et al. 2012; Forbes et al. 2012, 2014; Lilly et al. 2013; Dekel & Mandelker 2014; Tacchella et al. 2016; Rathaus & Sternberg 2016). **Figure 10** captures and summarizes the key aspects of this model by comparing the timescales (or rates) of this baryonic gas regulator system. As discussed in Section 3, the depletion time on the MS, which controls the maximum SFR in galaxies, has a time/redshift dependence that is plausibly tied to the dynamical time, or Toomre time, in a $Q < 1$ globally unstable disk, which in turn is tied to the Hubble time at z, $H(z)^{-1}$. The empirically determined time for doubling the stellar component, t_*, is approximately three to four times smaller (or the growth rate is three to four times faster) than the corresponding growth time of the dark matter halo in which the galaxy is embedded. At small masses, the efficiency of galaxy formation is low, due to very efficient stellar feedback.

For $z < z_{\text{peak}} \sim 2$, the gas consumption time is shorter than t_*, and the growth of the galaxy is tied to the cosmic baryon accretion rate, plus consumption of the gas reservoir, which is initially substantial but then is used up at $z < 0.2$. This means that in the local Universe, where t_* is longer than the Hubble time, all but the smallest galaxies stop growing (i.e., are starved), with the exception of gas returned by stars, and when H I from the outer disks is brought into the inner regions. However, for $z > z_{\text{peak}}$, the gas consumption time is longer than t_*. In this limit, the SFR is determined by the depletion time, and a significant fraction of the baryonic accretion builds up the internal gas reservoir (Lilly et al. 2013).

Galaxies are richest in molecular gas at redshifts somewhat lower than the epoch of maximum cosmic SFR. A possible explanation is that mass loading of galactic winds at early times and in small galaxies is high. Much of this recycled gas returns at later cosmic times ($z \sim 1$–2) into more massive galaxies, increasing their gas reservoirs and their SFRs above and beyond what would be expected from baryonic halo accretion (Oppenheimer et al. 2010). At all redshifts, diffuse gas accretion and minor mergers dominate the growth rate from major mergers by a substantial factor (e.g., Genel et al. 2008, 2009, 2010; Fakhouri & Ma 2008, 2009; Dekel et al. 2009a). Minor mergers can play a significant role at $z > 2.5$–5, but not at and below the peak of cosmic galaxy formation (Bouché et al. 2010; Davé et al. 2012; Lilly et al. 2013, figure 4; Dekel & Mandelker 2014).

Galaxies move up and down in the stellar mass–SFR plane on a timescale of a fraction of the Hubble time (Tacchella et al. 2016) because of the combination of perturbation by the disk instabilities; mergers; and changes in the orientation, geometry, and angular momentum of the cosmic streams feeding the galaxy. At $z > 1.5$, global disk instabilities and minor mergers transport gas
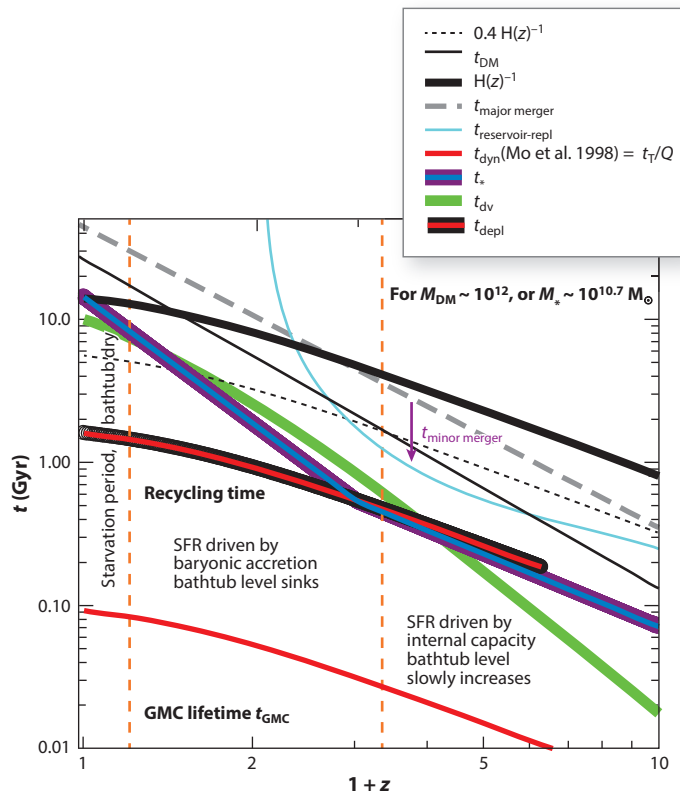
Figure 10

Summary of the various timescales affecting the galactic baryon cycle, plotted as a function of redshift and applicable for a 10^{12} $M_\odot$ halo. These timescales are (approximately from shortest to longest) the lifetime of a GMC (t_{GMC}), the dynamical time (t_{dyn}) or Toomre time (t_T) of a typical massive galaxy with angular momentum parameter $\lambda \sim 0.037$ (*red line*), the dynamical friction or viscous timescale (t_{dv}) for radial gas transport inside the galaxy (*green line*), the stellar growth time (t_*) (*thick blue-purple line*), the molecular gas depletion timescale (t_{depl}) (*thick red-black line*), the growth time of the dark matter halo (t_{DM}) (*thin black line*), the molecular gas reservoir replenishment time ($t_{reservoir-repl}$) (*cyan*), the typical time for up–down movement in the MS plane [$0.4\,H(z)^{-1}$] (*thin black dashed line*), the time between major mergers ($t_{major\ merger}$) (*thick gray dashed line*), the time for minor mergers ($t_{minor\ merger}$) (*purple arrow*) downward from that line, and the Hubble time [$H(z)^{-1}$] (*thick black line*). The epoch of recycling is at $z \sim 1$–2, with a typical time of 0.5 Gyr. The orange vertical dashed lines indicate the times in the equilibrium growth model when the SFR is driven by the available reservoir (at high redshifts), when it is driven by accretion (near the peak of cosmic star formation), and when the reservoir is running dry (at low redshifts). Abbreviations: GMC, giant molecular cloud; MS, main sequence; SFR, star-formation rate.

(and stars) radially inward on the viscous timescale, which is only ∼1 Gyr or less, because of the high gas fractions and gravitationally driven turbulence. This scale is comparable to the depletion and baryonic times, resulting in efficient buildup of central star-forming bulges.

6.3. Measurement Tools and Methods

We have addressed how one can most reliably determine the molecular gas content of galaxies, and how one can most efficiently and with minimal bias survey the molecular gas content of a cosmic volume. Far-IR and submillimeter dust emission are now available as tracers to check and, in some

instances, replace the classical CO luminosity method by being more time efficient (Bolatto et al. 2013; Scoville et al. 2014, 2017). We have shown that, apart from zero-point offsets, the three techniques give similar scaling relations, mitigating concerns about uncertain conversion factors. Pointed molecular gas observations of individual galaxies (or stacks) selected from the multiband deep imaging surveys and deep field scanning observations yield comparable evolutions of the molecular gas volume density as a function of redshift or of redshift and mass.

A major problem with the CO method, and probably also with the dust methods, is that emissivity (per mass) depends inversely on metallicity, such that it is hard or impossible to detect low-mass galaxies with substantially subsolar metallicity, and even harder to determine their gas content quantitatively. As a result, so far there have been few CO or dust detections of low-mass galaxies [$\log(M_*/M_\odot) \ll 10$] at high z. It is not obvious how substantial progress can be made in this area. Another unknown is whether an important ISM component is completely missing or overlooked with the current techniques, such as gas/dust at very low temperature.

6.4. Comparison of Observations and Theoretical Research

We have compared the empirical data with a range of semianalytic and hydrodynamic simulation–based theoretical papers. Broadly, both theoretical (typically calibrated on $z = 0$ results) and observational research on galaxy- and mass-integrated molecular and atomic hydrogen content per cosmic volume agree reasonably well. Both find that, compared with atomic gas, molecular gas is subdominant at all redshifts but evolves rapidly with redshift, peaking near but at somewhat lower redshift than the $z \sim 1$–3 cosmic SFR maximum. By studying in greater detail the mass functions, or ratios of gas to stellar mass, as a function of redshift, theoretical research predicts $z \sim 1$–2 massive galaxies near the Schechter mass to be less rich in molecular gas, by a factor of several, than what has been found observationally, while there appears to be no disagreement at $z = 0$. All semianalytic models and simulation-based research predict the majority of the molecular gas to be associated with lower-mass galaxies. Given the difficulty of detecting molecular gas in these lower-mass systems at $z \sim 1$–3 with any of the three observational techniques, it is not clear whether there is also tension at the low-mass tail. Moreover, the same result is obtained when the cosmic SFR luminosity functions (Madau & Dickinson 2014) are converted to molecular mass functions with an adopted depletion time scaling relation (**Figure 8**). This overall consistency is encouraging. The complexity of the combined effects of recycling and subgalactic processes may be at the core of the tension between simulations and observations.

6.5. Outlook for the Next Decade

In our opinion, there are likely three main avenues of research in which very fruitful progress can be expected in the next decade:

1. One is the extension to higher redshift. Will the physical phenomena we encounter on this journey be characterized primarily by straightforward extrapolation of the gas regulator system to earlier times, where rates are faster but the gas-to-star converters are on average smaller and less efficient in terms of lower intake and consumption, as well as higher mass loaded outflows (**Figure 10**)? The hydrodynamic simulations suggest that, prior to the cosmic SFR peak at $z \sim 3$–6, galaxies were much less settled in rotationally stabilized disks and much more perturbed by mergers, resulting in a more irregular growth, akin to that of lower-mass and dwarf galaxies at later cosmic times (e.g., Wetzel et al. 2016, Simons et al. 2017, Feldmann et al. 2019). JWST is scheduled to launch in 2021, shortly after the publication of this review, and will provide a plethora of high-z SFG targets for subsequent

studies of the gas and star-formation evolution at the earliest epochs of galaxy formation. The combination of ALMA and JWST in particular will lead to much progress, but a significant and coordinated investment of time of both facilities will be necessary to obtain robust statistical results.

2. The second obvious avenue will be spatially resolved studies, in particular those exploring the gas regulation and consumption processes on cloud and star cluster scales at $z \sim 1$–3. A clear lesson of the last decade has been that subgalactic-scale processes can radiate back out and determine SFRs, gas densities, outflows, metallicities, and perhaps even dark matter distribution on the scales of the outer disks and the CGM. Again, JWST, ALMA/NOEMA, and the 30-m-class optical/IR telescopes will be ideally suited for this task. Important research will focus on the radial transport and buildup of early gas-rich bulges that are predicted in the model of globally unstable disks, and for which first observations are becoming available.

3. The third avenue will be to connect molecular gas processes and kinematics with the incoming and outgoing ionized gas in the CGM and with the atomic gas in the outer disk. It is highly desirable to image the baryonic gas of selected galaxies in all phases (molecular, atomic, ionized, and very hot), initially in modest-redshift galaxies, where such imagery is possible with the pre-SKA precursors and where CGM tracers can be imaged in emission. Careful coordination between the relevant large telescopes will be required for such ambitious multiwavelength research to succeed and yield statistically robust answers.

Naturally, the universal baryon cycle model may not always be applicable. We have mentioned the $z > 3$ epoch where this model may fail and be replaced by a much more random set of consecutive merger events. There are also cases of star formation in extreme environments, such as in tidal tail dwarfs and in jet-induced star formation, and there are recent observations of molecular gas in the CGM, where the model may also be inapplicable. One might ask whether gas-rich but star-formation-poor galaxies exist. If so, deep multiband surveys in the submillimeter continuum (as an extinction-free indicator of SFR and dust mass) may be required to identify candidates.

DISCLOSURE STATEMENT

ACKNOWLEDGMENTS

LITERATURE CITED

Abdo AA, Ackermann M, Ajello M, et al. 2010. *Astrophys. J.* 710:133
Ali ZS, Parsons AR, Zheng H, et al. 2015. *Astrophys. J.* 809:61

Alves J, Lombardi M, Lada CJ. 2007. *Astron. Astrophys*. 462:17

André P, Men'shchikov A, Bontemps S, et al. 2010. *Astron. Astrophys*. 518:102

Anglés-Alcázar D, Faucher-Giguère C-A, Kereš D, et al. 2017. *MNRAS* 470:4698

Aravena M, Decarli R, Gónzalez-López J, et al. 2019. *Astrophys. J.* 882:136

Aravena M, Decarli R, Walter F, et al. 2016. *Astrophys. J.* 833:68

Aravena M, Hodge JA, Wagg J, et al. 2014. *MNRAS* 442:558

Arimoto N, Sofue Y, Tsujimoto T. 1996. *Publ. Astron. Soc. Jpn*. 48:275

Armus L, Mazzarella JM, Evans AS, et al. 2009. *Publ. Astron. Soc. Pac*. 121:559

Asplund M, Grevesse N, Sauval AJ, Allende Prieto C, Kiselman D. 2004. *Astron. Astrophys*. 417:751

Barro G, Faber SM, Pérez-González PG, et al. 2013. *Astrophys. J.* 765:104

Barro G, Kriek M, Pérez-González PG, et al. 2016. *Astrophys. J.* 827:32

Bauermeister A, Blitz L, Bolatto A, et al. 2013. *Astrophys. J.* 763:64

Beckwith SVW, Stiavelli M, Koekemoer AM, et al. 2006. *Astron. J.* 132:1729

Behrendt M, Burkert A, Schartmann M. 2015. *MNRAS* 448:1007

Behroozi PS, Conroy C, Wechsler RH. 2010. *Astrophys. J.* 717:379

Behroozi PS, Wechsler RH, Conroy C. 2013. *Astrophys. J.* 770:57

Bekki K. 2013. *MNRAS* 432:2298

Bell EF, van der Wel A, Papovich C, et al. 2012. *Astrophys. J.* 753:167

Berta S, Lutz D, Genzel R, Förster Schreiber NM, Tacconi LJ. 2016. *Astron. Astrophys*. 587:73

Bertemes C, Wuyts S, Lutz D, et al. 2018. *MNRAS* 478:1442

Béthermin M, Daddi E, Magdis G, et al. 2015. *Astron. Astrophys*. 573:113

Bezanson R, van der Wel A, Straatman C, et al. 2018. *Astrophys. J.* 868:36

Bialy S, Sternberg A. 2015. *MNRAS* 450:4424

Bialy S, Sternberg A. 2019. *Astrophys. J.* 881:160

Bigiel F, Leroy A, Walter F, et al. 2008. *Astron. J.* 136:2846

Bigiel F, Leroy AK, Walter F, et al. 2011. *Astrophys. J.* 730:13

Binney J, Tremaine S. 2008. *Galactic Dynamics*. Princeton, NJ: Princeton Univ. Press. 2nd ed.

Bisbas TG, Papadopoulos PP, Viti S. 2015. *Astrophys. J.* 803:37

Bisbas TG, van Dishoeck EF, Papadopoulos PP, et al. 2017. *Astrophys. J.* 839:90

Blain AW, Barnard VE, Chapman S. 2003. *MNRAS* 338:733

Blitz L, Rosolowsky E. 2006. *Astrophys. J.* 650:933

Bolatto AD, Leroy AK, Rosolowsky E, et al. 2008. *Astrophys. J.* 686:948

Bolatto AD, Wolfire M, Leroy AK. 2013. *Annu. Rev. Astron. Astrophys*. 51:207

Bolatto AD, Wong T, Utomo D, et al. 2017. *Astrophys. J.* 846:159

Boselli A, Eales S, Cortese L, et al. 2010. *Publ. Astron. Soc. Pac*. 122:261

Boselli A, Gavazzi G. 2014. *Astron. Astrophys. Rev.* 22:74

Bothwell MS, Smail I, Chapman SC, et al. 2013. *MNRAS* 429:3047

Bouché N, Dekel A, Genzel R, et al. 2010. *Astrophys. J.* 718:1001

Bournaud F, Elmegreen BG. 2009. *Astrophys. J.* 694:158

Bournaud F, Elmegreen BG, Martig M. 2009. *Astrophys. J. Lett.* 707:L1

Bouwens RJ, Bradley L, Zitrin A, et al. 2014. *Astrophys. J.* 795:126

Bower RG, Schaye J, Frenk CS, et al. 2017. *MNRAS* 465:32

Brammer GB, van Dokkum PG, Franx M, et al. 2012. *Astrophys. J. Suppl.* 200:13

Braun R. 2012. *Astrophys. J.* 749:87

Breysse PC, Rahman M. 2017. *MNRAS* 468:741

Brinchmann J, Charlot S, White SDM, et al. 2004. *MNRAS* 351:1151

Brusa M, Bongiorno A, Cresci G, et al. 2015. *MNRAS* 446:2394

Burkert A, Förster Schreiber NM, Genzel R, et al. 2016. *Astrophys. J.* 826:214

Carilli CL, Walter F. 2013. *Annu. Rev. Astron. Astrophys*. 51:105

Casey CM, Narayanan D, Cooray A. 2014. *Phys. Rep.* 541:45

Catinella B, Saintonge A, Janowiecki S, et al. 2018. *MNRAS* 476:875

Chabrier G. 2003. *Publ. Astron. Soc. Pac.* 115:763

Chevance M, Kruijssen JMD, Hygate APS, et al. 2020. *MNRAS* 493:2872

Christensen C, Quinn T, Governato F, Stilp A, Shen S, Wadsley J. 2012. *MNRAS* 425:3058

Combes F. 2018. *Astron. Astrophys. Rev.* 26:5

Combes F, García-Burillo S, Braine J, et al. 2011. *Astron. Astrophys.* 528:124

Combes F, García-Burillo S, Braine J, et al. 2013. *Astron. Astrophys.* 550:41

Cowie LL, González-López J, Barger AJ, et al. 2018. *Astrophys. J.* 865:106

Croton DJ, Springel V, White SDM, et al. 2006. *MNRAS* 365:11

Crutcher RM. 2012. *Annu. Rev. Astron. Astrophys.* 50:29

Daddi E, Bournaud F, Walter F, et al. 2010a. *Astrophys. J.* 713:686

Daddi E, Dannerbauer H, Liu D, et al. 2015. *Astron. Astrophys.* 577:46

Daddi E, Dickinson M, Morrison G, et al. 2007. *Astrophys. J.* 670:156

Daddi E, Elbaz D, Walter F, et al. 2010b. *Astrophys. J. Lett.* 714:L118

Daddi E, Renzini A, Pirzkal N, et al. 2005. *Astrophys. J.* 626:680

Dale DA, Helou G. 2002. *Astrophys. J.* 576:159

Dame TM, Hartmann D, Thaddeus P. 2001. *Astrophys. J.* 547:792

Dannerbauer H, Daddi E, Riechers DA, et al. 2009. *Astrophys. J. Lett.* 698:L178

Darvish B, Scoville NZ, Martin C, et al. 2018. *Astrophys. J.* 860:111

Davé R, Finlator K, Oppenheimer BD. 2011a. *MNRAS* 416:1354

Davé R, Finlator K, Oppenheimer BD. 2012. *MNRAS* 421:98

Davé R, Oppenheimer BD, Finlator K. 2011b. *MNRAS* 415:11

Davé R, Rafieferantsoa MH, Thompson RJ, Hopkins PF. 2017. *MNRAS* 467:115

Davé R, Thompson R, Hopkins PF. 2016. *MNRAS* 462:3265

DeBoer DR, Parsons AR, Aguirre JE, et al. 2017. *Publ. Astron. Soc. Pac.* 129:974

Decarli R, Walter F, Aravena M, et al. 2016. *Astrophys. J.* 833:70

Decarli R, Walter F, Carilli C, et al. 2014. *Astrophys. J.* 782:78

Decarli R, Walter F, Gónzalez-López J, et al. 2019. *Astrophys. J.* 882:138

Dekel A, Birnboim Y. 2006. *MNRAS* 368:2

Dekel A, Birnboim Y, Engel G, et al. 2009a. *Nature* 457:451

Dekel A, Krumholz MR. 2013. *MNRAS* 432:455

Dekel A, Mandelker N. 2014. *MNRAS* 444:2071

Dekel A, Sari R, Ceverino D. 2009b. *Astrophys. J.* 703:785

Delvecchio I, Lutz D, Berta S, et al. 2015. *MNRAS* 449:373

Dickey JM, Brinks E. 1993. *Astrophys. J.* 405:153

Dickman RL, Snell RL, Schloerb FP. 1986. *Astrophys. J.* 309:326

Diemer B, Stevens ARH, Forbes JC, et al. 2018. *Astrophys. J. Suppl.* 238:33

Dobbs CL, Burkert A, Pringle JE. 2011. *MNRAS* 413:2935

Dobbs CL, Pringle JE. 2013. *MNRAS* 432:653

Downes D, Eckart A. 2007. *Astron. Astrophys.* 468:57

Downes D, Solomon PM. 1998. *Astrophys. J.* 507:615

Draine BT. 1978. *Astrophys. J. Suppl.* 36:595

Draine BT, Dale DA, Bendo G, et al. 2007. *Astrophys. J.* 663:866

Draine BT, Li A. 2007. *Astrophys. J.* 657:810

Dunlop JS, McLure RJ, Biggs AD, et al. 2017. *MNRAS* 466:861

Eales S, de Vis P, Smith MWL, et al. 2017. *MNRAS* 465:3125

Eales S, Dunne L, Clements D, et al. 2010. *Publ. Astron. Soc. Pac.* 122:499

Eales S, Fullard A, Allen M, et al. 2015. *MNRAS* 452:3489

Elbaz D, Daddi E, Le Borgne D, et al. 2007. *Astron. Astrophys.* 468:33

Elbaz D, Dickinson M, Hwang HS, et al. 2011. *Astron. Astrophys.* 533:119

Elmegreen BG. 1993. *Astrophys. J.* 411:170

Elmegreen BG. 1997. *Rev. Mex. Astron. Astrofis.* 6:165

Elmegreen BG. 2002. *Astrophys. J.* 577:206

Elmegreen BG. 2007. *Astrophys. J.* 668:1064

Elmegreen BG, Scalo J. 2004. *Annu. Rev. Astron. Astrophys.* 42:211

Engel H, Tacconi LJ, Davies RI, et al. 2010. *Astrophys. J.* 724:233

Epinat B, Tasca L, Amram P, et al. 2012. *Astron. Astrophys.* 539:92

Escala A. 2011. *Astrophys. J.* 735:56

Faber SM, Willmer C, Wolf C, et al. 2007. *Astrophys. J.* 665:265

Faerman Y, Sternberg A, McKee CF. 2017. *Astrophys. J.* 835:52

Fakhouri O, Ma C-P. 2008. *MNRAS* 386:577

Fakhouri O, Ma C-P. 2009. *MNRAS* 394:1825

Fall SM, Romanowsky AJ. 2013. *Astrophys. J.* 769:26

Faucher-Giguère C-A, Quataert E. 2012. *MNRAS* 425:605

Feldmann R, Faucher-Giguère C-A, Kereš D. 2019. *Astrophys. J.* 871:21

Feldmann R, Gnedin NY, Kravtsov AV. 2012a. *Astrophys. J.* 747:124

Feldmann R, Gnedin NY, Kravtsov AV. 2012b. *Astrophys. J.* 758:127

Field GB, Goldsmith DW, Habing HJ. 1969. *Astrophys. J.* 155:149

Forbes JC, Krumholz M, Burkert A. 2012. *Astrophys. J.* 754:48

Forbes JC, Krumholz MR, Burkert A, Dekel A. 2014. *MNRAS* 438:1552

Förster Schreiber NM, Genzel R, Bouché N, et al. 2009. *Astrophys. J.* 706:1364

Förster Schreiber NM, Genzel R, Lehnert MD, et al. 2006. *Astrophys. J.* 645:1062

Förster Schreiber NM, Übler H, Davies RL, et al. 2019. *Astrophys. J.* 875:21

Förster Schreiber NM, Wuyts S. 2020. *Annu. Rev. Astron. Astrophys.* 58:661

Franco M, Elbaz D, Béthermin M, et al. 2018. *Astron. Astrophys.* 620:152

Frayer DT, Harris AI, Baker AJ, et al. 2011. *Astrophys. J.* 726:22

Frayer DT, Ivison RJ, Scoville NZ, et al. 1998. *Astrophys. J. Lett.* 506:L7

Frayer DT, Ivison RJ, Scoville NZ, et al. 1999. *Astrophys. J. Lett.* 514:L13

Freundlich J, Combes F, Tacconi LJ, et al. 2019. *Astron. Astrophys.* 622:105

Fu J, Guo Q, Kauffmann G, Krumholz MR. 2010. *MNRAS* 409:515

Fu J, Kauffmann G, Li C, Guo Q. 2012. *MNRAS* 424:2701

Fujimoto S, Ouchi M, Shibuya T, Nagai H. 2017. *Astrophys. J.* 850:83

Galametz M, Madden SC, Galliano F, et al. 2011. *Astron. Astrophys.* 532:56

Gao Y, Carilli CL, Solomon PM, Vanden Bout PA. 2007. *Astrophys. J. Lett.* 660:L93

Gao Y, Solomon PM. 2004. *Astrophys. J.* 606:271

Garcia-Burillo S, Usero A, Alonso-Herrero A, et al. 2012. *Astron. Astrophys.* 539:8

Genel S, Bouché N, Naab T, Sternberg A, Genzel R. 2010. *Astrophys. J.* 719:229

Genel S, Genzel R, Bouché N, et al. 2008. *Astrophys. J.* 688:789

Genel S, Genzel R, Bouché N, Naab T, Sternberg A. 2009. *Astrophys. J.* 701:2002

Genel S, Vogelsberger M, Springel V, et al. 2014. *MNRAS* 445:175

Genzel R, Burkert A, Bouché N, et al. 2008. *Astrophys. J.* 687:59

Genzel R, Förster Schreiber NM, Lang P, et al. 2014. *Astrophys. J.* 785:75

Genzel R, Lutz D, Sturm E, et al. 1998. *Astrophys. J.* 498:579

Genzel R, Newman S, Jones T, et al. 2011. *Astrophys. J.* 733:101

Genzel R, Tacconi LJ, Combes F, et al. 2012. *Astrophys. J.* 746:69

Genzel R, Tacconi LJ, Gracia-Carpio J, et al. 2010. *MNRAS* 407:2091

Genzel R, Tacconi LJ, Lutz D, et al. 2015. *Astrophys. J.* 798:1

Giavalisco M, Ferguson HC, Koekemoer AM, et al. 2004. *Astrophys. J. Lett.* 600:L93

Gillmon K, Shull JM, Tumlinson J, Danforth C. 2006. *Astrophys. J.* 636:891

Gilmore G, Wyse RFG, Kuijken K. 1989. *Annu. Rev. Astron. Astrophys.* 27:555

Glover SCO, Clark PC. 2012. *MNRAS* 421:9

Gnedin NY. 2000. *Astrophys. J.* 542:535

Gnedin NY, Kravtsov AV. 2011. *Astrophys. J.* 728:88

González-López J, Decarli R, Pavesi R, et al. 2019. *Astrophys. J.* 882:139

Gracia-Carpio J. 2009. *The molecular gas in luminous and ultraluminous infrared galaxies*. PhD Thesis, Univ.
    Madrid, Spain

Gracia-Carpio J, Garcia-Burillo S, Planesas P, Fuente A, Usero A. 2008. *Astron. Astrophys.* 479:703

Gracia-Carpio J, Sturm E, Hailey-Dunsheath S, et al. 2011. *Astrophys. J. Lett.* 728:L7

Grenier IA, Casandjian J-M, Terrier R. 2005. *Science* 307:1292

Grogin NA, Kocevski DD, Faber SM, et al. 2011. *Astrophys. J. Suppl.* 197:35

Guimarães R, Petitjean P, de Carvalho RR, et al. 2009. *Astron. Astrophys.* 508:133

Guo Q, White SDM. 2008. *MNRAS* 384:2

Guo Q, White SDM, Boylan-Kolchin M, et al. 2011. *MNRAS* 413:101

Harrison CM, Alexander DM, Mullaney JR, et al. 2014. *MNRAS* 441:3306

Hatsukade B, Kohno K, Yamaguchi Y, et al. 2018. *Publ. Astron. Soc. Jpn.* 70:105

Hayashi M, Tadaki K, Kodama T, et al. 2018. *Astrophys. J.* 856:118

Haynes MP, Giovanelli R, Martin AM, et al. 2011. *Astron. J.* 142:170

Heckman TM, Robert C, Leitherer C, Garnett DR, van der Rydt F. 1998. *Astrophys. J.* 503:646

Heiles C, Troland TH. 2003. *Astrophys. J. Suppl.* 145:329

Herrera-Camus R, Bolatto AD, Wolfire MG, et al. 2015. *Astrophys. J.* 800:1

Herrera-Camus R, Tacconi L, Genzel R, et al. 2019. *Astrophys. J.* 871:37

Heiderman A, Evans NJ II, Allen LE, Huard T, Heyer M. 2010. *Astrophys. J.* 723:1019

Hickox RC, Mullaney JR, Alexander DM, et al. 2014. *Astrophys. J.* 782:9

Hodge JA, Karim A, Smail I, et al. 2013. *Astrophys. J.* 768:91

Hodge JA, Smail I, Walter F, et al. 2019. *Astrophys. J.* 876:130

Hodge JA, Swinbank AM, Simpson JM, et al. 2016. *Astrophys. J.* 833:103

Hopkins PF, Kereš D, Oñorbe J, et al. 2014. *MNRAS* 445:581

Hu CY, Naab T, Walch S, Glover SCO, Clark PC. 2016. *MNRAS* 458:3258

Huang M-L, Kauffmann G. 2014. *MNRAS* 443:1329

Ilbert O, McCracken HJ, Le Fèvre O, et al. 2013. *Astron. Astrophys.* 556:551

Ilbert O, Salvato M, Le Floc'h E, et al. 2010. *Astrophys. J.* 709:644

Immeli A, Samland M, Gerhard O, Westera P. 2004. *Astron. Astrophys.* 413:547

Israel FP. 1997. *Astron. Astrophys.* 328:471

Israel FP. 2000. In *Molecular Hydrogen in Space*, ed. F Combes, G Pineau des Forêts, p. 293. Cambridge, UK: Cambridge Univ. Press

Ivison RJ, Papadopoulos PP, Smail I, et al. 2011. *MNRAS* 412:1913

Jansen DJ, Spaans M Hogerheijde MR, van Dishoeck EF. 1995. *Astron. Astrophys.* 303:541

Kaasinen M, Scoville N, Walter F, et al. 2019. *Astrophys. J.* 880:15

Karim A, Schinnerer E, Martínez-Sansigre A, et al. 2011. *Astrophys. J.* 730:61

Kauffmann G, Heckman TM, White SDM, et al. 2003. *MNRAS* 341:54

Kauffmann G, White SDM, Guiderdoni B. 1993. *MNRAS* 264:201

Kauffmann G, White SDM, Heckman TM, et al. 2004. *MNRAS* 353:713

Kassin SA, Weiner BJ, Faber SM, et al. 2007. *Astrophys. J.* 660:35

Kassin SA, Weiner BJ, Faber SM, et al. 2012. *Astrophys. J.* 758:106

Keating GK, Marrone DP, Bower GC. 2016. *Astrophys. J.* 830:34

Kenney JDP, Young JS. 1989. *Astrophys. J.* 344:171

Kennicutt RC Jr. 1989. *Astrophys. J.* 344:685

Kennicutt RC Jr. 1998. *Astrophys. J.* 498:541

Kennicutt RC Jr., Calzetti D, Walter F, et al. 2007. *Astrophys. J.* 671:333

Kennicutt RC Jr., Evans N. 2012. *Annu. Rev. Astron. Astrophys.* 50:531

Keres D, Yun MS, Young JS. 2003. *Astrophys. J.* 582:659

Klessen RS, Heitsch F, Mac Low M-M. 2000. *Astrophys. J.* 535:887

Koekemoer AM, Faber SM, Ferguson HC, et al. 2011. *Astrophys. J. Suppl.* 197:36

Könyves V, André P, Men'shchikov A, et al. 2015. *Astron. Astrophys.* 584:91

Kovetz ED, Viero MP, Lidz A, et al. 2017. arXiv:1709.09066 [astro-ph.CO]

Koyama S, Koyama Y, Yamashita T, et al. 2017. *Astrophys. J.* 847:137

Kravtsov AV, Berlind AA, Wechsler RH, et al. 2004. *Astrophys. J.* 609:35

Kroupa P. 2001. *MNRAS* 322:231

Kruijssen JMD, Schruba A, Chevance M, et al. 2019. *Nature* 569:519

Krumholz MR, Burkhart B, Forbes JC, Crocker RM. 2018. *MNRAS* 477:2716

Krumholz MR, Dekel A, McKee CF. 2012. *Astrophys. J.* 745:69

Krumholz MR, Leroy AK, McKee CF. 2011. *Astrophys. J.* 731:25

Krumholz MR, McKee CF. 2005. *Astrophys. J.* 630:250

Krumholz MR, McKee CF, Tumlinson J. 2008. *Astrophys. J.* 689:865

Krumholz MR, McKee CF, Tumlinson J. 2009. *Astrophys. J.* 699:850

Krumholz MR, Tan JC. 2007. *Astrophys. J.* 654:304

Kuhlen M, Krumholz MR, Madau P, Smith BD, Wise J. 2012. *Astrophys. J.* 749:36

Lacy JH, Knacke R, Geballe TR, Tokunaga AT. 1994. *Astrophys. J. Lett.* 428:L69

Lacy JH, Sneden C, Kim H, Jaffe DT. 2017. *Astrophys. J.* 838:66

Lada CJ, Forbrich J, Lombardi M, Alves JF. 2012. *Astrophys. J.* 745:190

Lagos CDP, Baugh CM, Lacey CG, et al. 2011. *MNRAS* 418:1649

Lagos CDP, Bayet E, Baugh CM, et al. 2012. *MNRAS* 426:2142

Lagos CDP, Crain RA, Schaye J, et al. 2015. *MNRAS* 452:3815

Lang P, Wuyts S, Somerville R, et al. 2014. *Astrophys. J.* 788:11

Larson RB. 1981. *MNRAS* 194:809

Lee MM, Tanaka I, Kawabe R, et al. 2017. *Astrophys. J.* 842:55

Lee Y, Snell RL, Dickman RL. 1990. *Astrophys. J.* 355:536

Lenkic L, Bolatto AD, Förster Schreiber NM, et al. 2020. *Astron. J.* 159:190

Leroy AK, Bolatto A, Gordon K, et al. 2011. *Astrophys. J.* 737:12

Leroy AK, Walter F, Bigiel F, et al. 2009. *Astron. J.* 137:4670

Leroy AK, Walter F, Brinks E, et al. 2008. *Astron. J.* 136:2782

Leroy AK, Walter F, Sandstrom K, et al. 2013. *Astron. J.* 146:19

Li TY, Wechsler RH, Devaraj K, Church SE. 2016. *Astrophys. J.* 817:169

Lidz A, Furlanetto SR, Oh SP, et al. 2011. *Astrophys. J.* 741:L70

Lilly SJ, Carollo CM, Pipino A, Renzini A, Peng Y. 2013. *Astrophys. J.* 772:119

Lilly SJ, LeFevre O, Hammer F, Crampton D. 1996. *Astrophys. J.* 460:1

Lupi A, Bovino S, Capelo PR, Volonteri M, Silk J. 2018. *MNRAS* 474:2884

Lutz D, Poglitsch A, Altieri B, et al. 2011. *Astron. Astrophys.* 532:90

Mac Low M-M. 1999. *Astrophys. J.* 524:169

Madau P, Dickinson M. 2014. *Annu. Rev. Astron. Astrophys.* 52:415

Madau P, Ferguson HC, Dickinson ME, et al. 1996. *MNRAS* 283:1388

Magdis GE, Daddi E, Béthermin M, et al. 2012a. *Astrophys. J.* 760:6

Magdis GE, Daddi E, Sargent M, et al. 2012b. *Astrophys. J.* 758:9

Magdis GE, Elbaz D, Dickinson M, et al. 2011. *Astron. Astrophys.* 534:15

Magdis GE, Rigopoulou D, Daddi E, et al. 2017. *Astron. Astrophys.* 603:93

Magnelli B, Lutz D, Saintonge A, et al. 2014. *Astron. Astrophys.* 561:86

Magnelli B, Saintonge A, Lutz D, et al. 2012. *Astron. Astrophys.* 548:22

Marinacci F, Grand RJJ, Pakmor R, et al. 2017. *MNRAS* 466:3859

Martin CL, Scannapieco E, Ellison SL, et al. 2010. *Astrophys. J.* 721:174

Mashian N, Sternberg A, Loeb A. 2015. *J. Cosmol. Astropart. Phys.* 11:28

McKee CF, Krumholz M. 2010. *Astrophys. J.* 709:308

McKee CF, Ostriker EC. 2007. *Annu. Rev. Astron. Astrophys.* 45:565

Meidt SE, Leroy AK, Rosolowsky E, et al. 2018. *Astrophys. J.* 854:100

Michałowski MJ, Dunlop JS, Cirasuolo M, et al. 2012. *Astron. Astrophys.* 541:12

Mihos JC, Hernquist L. 1996. *Astrophys. J.* 464:641

Miville-Deschenes MA, Murray N, Lee EJ. 2017. *Astrophys. J.* 834:57

Mo HJ, Mao S, White SDM. 1998. *MNRAS* 295:319

Mok A, Wilson CD, Golding J, et al. 2016. *MNRAS* 456:4384

Momcheva IG, Brammer GB, van Dokkum PG, et al. 2016. *Astrophys. J. Suppl.* 225:27

Mortier AMJ, Serjeant S, Dunlop JS, et al. 2005. *MNRAS* 363:563

Moster BP, Naab T, White SDM. 2013. *MNRAS* 428:3121

Mouschovias TC. 1976. *Astrophys. J.* 207:141

Mullaney JR, Pannella M, Daddi E, et al. 2012. *MNRAS* 419:95

Murray N, Quataert E, Thompson TA. 2005. *Astrophys. J.* 618:569

Naab T, Ostriker JP. 2017. *Annu. Rev. Astron. Astrophys.* 55:59

Narayanan D, Krumholz M, Ostriker EC, Hernquist L. 2011. *MNRAS* 418:664

Narayanan D, Krumholz M, Ostriker EC, Hernquist L. 2012. *MNRAS* 421:3127

Neistein E, Dekel A. 2008. *MNRAS* 388:1792

Nelson D, Pillepich A, Springel V, et al. 2019. *MNRAS* 490:3234

Newman SF, Genzel R, Förster Schreiber NM, et al. 2013. *Astrophys. J.* 767:104

Nickerson S, Teyssier R, Rosdahl J. 2018. *MNRAS* 479:3206

Nickerson S, Teyssier R, Rosdahl J. 2019. *MNRAS* 484:1238

Noble AG, McDonald M, Muzzin A, et al. 2017. *Astrophys. J. Lett.* 842:L21

Noeske KG, Weiner BJ, Faber SM, et al. 2007. *Astrophys. J. Lett.* 660:L43

Noguchi M. 1999. *Astrophys. J.* 514:77

Nordon R, Lutz D, Genzel R, et al. 2012. *Astrophys. J.* 745:182

Nordon R, Sternberg A. 2016. *MNRAS* 462:2804

Noterdaeme P, Petitjean P, Carithers WC, et al. 2012. *Astron. Astrophys.* 547:1

Obreschkow D, Croton D, De Lucia G, Khochfar S, Rawlings S. 2009. *Astrophys. J.* 698:1467

Obreschkow D, Rawlings S. 2009a. *MNRAS* 394:1857

Obreschkow D, Rawlings S. 2009b. *Astrophys. J. Lett.* 696:L129

Oesch PA, Brammer G, van Dokkum PG, et al. 2016. *Astrophys. J.* 819:129

Oliver SJ, Bock J, Altieri B, et al. 2012. *MNRAS* 424:1614

Oppenheimer BD, Davé R, Kereš D, et al. 2010. *MNRAS* 406:2325

Ostriker EC, McKee CF, Leroy AK. 2010. *Astrophys. J.* 721:975

Ostriker EC, Shetty R. 2011. *Astrophys. J.* 731:41

Papadopoulos PP, Bisbas TG, Zhang Z-Y. 2018. *MNRAS* 478:1716

Parmar PS, Lacy JH, Achtermann JM. 1991. *Astrophys. J. Lett.* 372:L25

Patil P, Nyland K, Lacy M, et al. 2019. *Astrophys. J.* 871:109

Pavesi R, Sharon CE, Riechers DA, et al. 2018. *Astrophys. J.* 864:49

Peng Y, Lilly SJ, Kovač K, et al. 2010. *Astrophys. J.* 721:193

Peng Y, Maiolino R. 2014. *MNRAS* 443:3643

Peng Y, Maiolino R, Cochrane R. 2015. *Nature* 521:192

Péroux C, Dessauges-Zavadsky M, D'Odorico S, Sun KT, McMahon RG. 2005. *MNRAS* 363:479

Péroux C, Howk JC. 2020. *Annu. Rev. Astron. Astrophys.* 58:363

Pettini M, Pagel BEJ. 2004. *MNRAS* 348:59

Pillepich A, Nelson D, Springel V, et al. 2019. *MNRAS* 490:3196

Popping G, Caputi KI, Trager SC, et al. 2015. *MNRAS* 454:2258

Popping G, Pillepich A, Somerville RS, et al. 2019. *Astrophys. J.* 882:137

Popping G, Somerville RS, Trager SC. 2014. *MNRAS* 442:2398

Prochaska JX, Wolfe AM. 2009. *Astrophys. J.* 696:1543

Rachford BL, Snow TP, Destree JD, et al. 2009. *Astrophys. J. Suppl.* 180:125

Rachford BL, Snow TP, Tumlinson J, et al. 2002. *Astrophys. J.* 577:221

Rao SM, Turnshek DA, Nestor DB. 2006. *Astrophys. J.* 636:610

Rathaus B, Sternberg A. 2016. *MNRAS* 458:3168

Rees MJ, Ostriker JP. 1977. *MNRAS* 179:541

Rémy-Ruyer A, Madden SC, Galliano F, et al. 2014. *Astron. Astrophys.* 563:31

Renzini A, Peng Y. 2015. *Astrophys. J.* 801:29

Rhee J, Lah P, Briggs FH, et al. 2018. *MNRAS* 473:1879

Richter MJ, Graham JR, Wright GS, Kelly DM, Lacy JH. 1995. *Astrophys. J. Lett.* 449:L83

Rickard LJ, Palmer P, Morris M, Turner BE, Zuckerman B. 1977. *Astrophys. J.* 213:673

Rickard LJ, Palmer P, Morris M, Zuckerman B, Turner BE. 1975. *Astrophys. J. Lett.* 199:L75

Riechers DA, Carilli CL, Walter F, Momjian E. 2010. *Astrophys. J. Lett.* 724:L153
Riechers DA, Pavesi R, Sharon CE, et al. 2019. *Astrophys. J.* 872:7
Rieke GH, Lebofsky MJ, Thompson RI, Low FJ, Tokunaga AT. 1980. *Astrophys. J.* 238:24
Rieke GH, Loken K, Rieke MJ, Tamblyn P. 1993. *Astrophys. J.* 412:99
Righi M, Hernández-Monteagudo C, Sunyaev RA. 2008. *Astron. Astrophys.* 489:489
Robertson BE, Kravtsov AV. 2008. *Astrophys. J.* 680:1083
Rodighiero G, Brusa M, Daddi E, et al. 2015. *Astrophys. J.* 800:10
Rodighiero G, Cimatti A, Gruppioni C, et al. 2010. *Astron. Astrophys.* 518:25
Rodighiero G, Daddi E, Baronchelli I, et al. 2011. *Astrophys. J.* 739:40
Romanowsky AJ, Fall SM. 2012. *Astrophys. J. Suppl.* 203:17
Romeo AB, Mogotsi KM. 2017. *MNRAS* 469:286
Rowan-Robinson M, Crawford J. 1989. *MNRAS* 238:523
Rudnick G, Hodge J, Walter F, et al. 2017. *Astrophys. J.* 849:27
Saintonge A, Catinella B, Cortese L, et al. 2016. *MNRAS* 462:1749
Saintonge A, Catinella B, Tacconi LJ, et al. 2017. *Astrophys. J. Suppl.* 233:22
Saintonge A, Kauffmann G, Kramer C, et al. 2011a. *MNRAS* 415:32
Saintonge A, Kauffmann G, Wang J, et al. 2011b. *MNRAS* 415:61
Saintonge A, Lutz D, Genzel R, et al. 2013. *Astrophys. J.* 778:2
Sanders DB, Mirabel IF. 1996. *Annu. Rev. Astron. Astrophys.* 34:749
Sanders DB, Soifer BT, Elias JH, et al. 1988. *Astrophys. J.* 325:74
Santini P, Maiolino R, Magnelli B, et al. 2014. *Astron. Astrophys.* 562:30
Sargent MT, Béthermin M, Daddi E, et al. 2014. *Astrophys. J.* 793:19
Scalo J, Elmegreen BG. 2004. *Annu. Rev. Astron. Astrophys.* 42:275
Schaye J. 2004. *Astrophys. J.* 609:667
Schaye J, Crain RA, Bower RG, et al. 2015. *MNRAS* 446:521
Schiminovich D, Wyder TK, Martin DC, et al. 2007. *Astrophys. J. Suppl.* 173:315
Schinnerer E, Groves B, Sargent MT, et al. 2016. *Astrophys. J.* 833:112
Schreiber C, Pannella M, Elbaz D, et al. 2015. *Astron. Astrophys.* 757:74
Schruba A, Kruijssen JMD, Leroy AK. 2019. *Astrophys. J.* 883:2
Schruba A, Leroy AK, Walter F, et al. 2011. *Astron. J.* 142:37
Scoville NZ, Aussel H, Sheth K, et al. 2014. *Astrophys. J.* 783:84
Scoville NZ, Lee N, van den Bout P, et al. 2017. *Astrophys. J.* 837:150
Scoville NZ, Sheth K, Aussel H, et al. 2016. *Astrophys. J.* 820:83
Scoville NZ, Yun MS, Brown RL, Vanden Bout PA. 1995. *Astrophys. J. Lett.* 449:L109
Scoville NZ, Yun MS, Bryant PM. 1997. *Astrophys. J.* 484:702
Shapiro KL, Genzel R, Förster Schreiber NM, et al. 2008. *Astrophys. J.* 682:23
Sharon CE, Tagore AS, Baker AJ, et al. 2019. *Astrophys. J.* 879:52
Shu FH, Adams FC, Lizano S. 1987. *Annu. Rev. Astron. Astrophys.* 25:23
Shull JM, Tumlinson J, Jenkins EB, et al. 2000. *Astrophys. J.* 538:73
Silk J. 1997. *Astrophys. J.* 481:703
Silverman JD, Daddi E, Rodighiero G, et al. 2015. *Astrophys. J.* 812:23
Silverman JD, Rujopakarn W, Daddi E, et al. 2018. *Astrophys. J.* 867:92
Simons RC, Kassin SA, Weiner BJ, et al. 2017. *Astrophys. J.* 843:46
Skelton RE, Whitaker KE, Momcheva IG, et al. 2014. *Astrophys. J. Suppl.* 214:24
Smail I, Ivison RJ, Blain AW. 1997. *Astrophys. J. Lett.* 490:L5
Solomon PM, de Zafra R. 1975. *Astrophys. J. Lett.* 188:L79
Solomon PM, Downes D, Radford SJE, Barrett JW. 1997. *Astrophys. J.* 478:144
Solomon PM, Rivolo AR, Barrett J, Yahil A. 1987. *Astrophys. J.* 319:730
Somerville RS, Davé R. 2015. *Annu. Rev. Astron. Astrophys.* 53:51
Speagle JS, Steinhardt CL, Capak PL, Silverman JD. 2014. *Astrophys. J. Suppl.* 214:15
Spilker J, Bezanson R, Barišić I, et al. 2018. *Astrophys. J.* 860:103
Stacey GJ, Hailey-Dunsheath S, Ferkinhoff C, et al. 2010. *Astrophys. J.* 724:957

Stanimirović S, Murray CE, Lee MY, Heiles C, Miller J. 2014. *Astrophys. J.* 793:132
Steidel CC, Giavalisco M, Dickinson ME, Adelberger KL. 1996. *Astron. J.* 112:352
Sternberg A. 1988. *Astrophys. J.* 332:400
Sternberg A, Dalgarno A. 1989. *Astrophys. J.* 338:197
Sternberg A, Dalgarno A. 1995. *Astrophys. J. Suppl.* 99:565
Sternberg A, Le Petit F, Roueff E, Le Bourlot J. 2014. *Astrophys. J.* 790:10
Stone JM, Ostriker EC, Gammie CF. 1998. *Astrophys. J. Lett.* 508:L99
Stott JP, Swinbank AM, Johnson HL, et al. 2016. *MNRAS* 457:1888
Strong AW, Mattox JR. 1996. *Astron. Astrophys.* 308:L21
Suess KA, Bezanson R, Spilker JS, et al. 2017. *Astrophys. J. Lett.* 846:L14
Sun J, Leroy AK, Schruba A, et al. 2018. *Astrophys. J.* 860:172
Swinbank AM, Harrison CM, Trayford J, et al. 2017. *MNRAS* 467:3140
Tacchella S, Carollo CM, Renzini A, et al. 2015. *Science* 348:314
Tacchella S, Dekel A, Carollo CM, et al. 2016. *MNRAS* 457:2790
Tacconi LJ, Genzel R, Neri R, et al. 2010. *Nature* 463:781
Tacconi LJ, Genzel R, Saintonge A, et al. 2018. *Astrophys. J.* 853:179
Tacconi LJ, Genzel R, Smail I, et al. 2008. *Astrophys. J.* 680:246
Tacconi LJ, Neri R, Chapman SC, et al. 2006. *Astrophys. J.* 640:228
Tacconi LJ, Neri R, Genzel R, et al. 2013. *Astrophys. J.* 768:74
Tadaki K, Genzel R, Kodama T, et al. 2017. *Astrophys. J.* 834:135
Tadaki K, Kodama T, Hayashi M, et al. 2019. *Publ. Astron. Soc. Jpn.* 71:40
Thompson R, Nagamine K, Jaacks J, Choi J-H. 2014. *Astrophys. J.* 780:145
Tomassetti M, Porciani C, Romano-Díaz E, Ludlow AD. 2015. *MNRAS* 446:3330
Tomassetti M, Porciani C, Romano-Díaz E, Ludlow AD, Papadopoulos PP. 2014. *MNRAS* 445:124
Toomre A. 1964. *Astrophys. J.* 139:1217
Trujillo I, Feulner G, Goranova Y, et al. 2006. *MNRAS* 373:36
Tumlinson J, Shull JM, Rachford BL, et al. 2002. *Astrophys. J.* 566:857
Übler H, Genzel R, Tacconi LJ, et al. 2018. *Astrophys. J. Lett.* 854:L24
Übler H, Genzel R, Wisnioski E, et al. 2019. *Astrophys. J.* 880:48
Utomo D, Bolatto AD, Wong T, et al. 2017. *Astrophys. J.* 849:26
Valentino F, Magdis GE, Daddi E, et al. 2018. *Astrophys. J.* 869:27
Vallini L, Gruppioni C, Pozzi F, Vignali C, Zamorani G. 2016. *MNRAS* 456:40
Valtchanov I, Virdee J, Ivison RJ, et al. 2011. *MNRAS* 415:3473
van Dokkum PG, Franx M, Kriek M, et al. 2008. *Astrophys. J. Lett.* 677:L5
Vanden Bout PA, Solomon PM, Maddalena RJ. 2004. *Astrophys. J. Lett.* 614:L97
Walter F, Decarli R, Aravena M, et al. 2016. *Astrophys. J.* 833:67
Warren SR, Skillman ED, Stilp AM, et al. 2012. *Astrophys. J.* 757:84
Weiss A, Downes D, Walter F, Henkel C. 2007. In *From Z-Machines to ALMA*: (*Sub*)*Millimeter Spectroscopy of Galaxies*, ed. AJ Baker, J Glenn, AI Harris, JG Mangum, MS Yun, p. 25. San Francisco: Astron. Soc. Pac.
Weiss A, Kovács A, Coppin K, et al. 2009. *Astrophys. J.* 707:1201
Wetzel AR, Hopkins PF, Kim J, et al. 2016. *Astrophys. J.* 823:23
Whitaker KE, Franx M, Leja J, et al. 2014. *Astrophys. J.* 795:104
Whitaker KE, van Dokkum PG, Brammer G, Franx M. 2012. *Astrophys. J. Lett.* 754:L29
White SDM, Frenk CS. 1991. *Astrophys. J.* 379:52
White SDM, Rees MJ. 1978. *MNRAS* 183:341
Wiklind T, Conselice CJ, Dahlen T, et al. 2014. *Astrophys. J.* 785:111
Wiklind T, Ferguson HC, Guo Y, et al. 2019. *Astrophys. J.* 878:83
Williams RE, Blacker B, Dickinson M, et al. 1996. *Astron. J.* 112:1335
Williams RJ, Quadri RF, Franx M, van Dokkum P, Labbé I. 2009. *Astrophys. J.* 691:1879
Wilson CD. 1995. *Astrophys. J. Lett.* 448:L97
Wisnioski E, Förster Schreiber NM, Fossati M, et al. 2019. *Astrophys. J.* 886:124
Wisnioski E, Förster Schreiber NM, Wuyts S, et al. 2015. *Astrophys. J.* 799:209

Wolfire MG, Hollenbach D, McKee CF. 2010. *Astrophys. J.* 716:1191

Wolfire MG, McKee CF, Hollenbach D, Tielens AGGM. 2003. *Astrophys. J.* 587:278

Wong T, Blitz L. 2002. *Astrophys. J.* 569:157

Wuyts S, Förster Schreiber NM, Lutz D, et al. 2011a. *Astrophys. J.* 738:106

Wuyts S, Förster Schreiber NM, van der Wel A, et al. 2011b. *Astrophys. J.* 742:96

Xie L, De Lucia G, Hirschmann M, Fontanot F, Zoldan A. 2017. *MNRAS* 469:968

Young JS, Scoville NZ. 1991. *Annu. Rev. Astron. Astrophys.* 29:581

Zavala JA, Casey CM, da Cunha E, et al. 2018. *Astrophys. J.* 869:71

Zolotov A, Dekel A, Mandelker N, et al. 2015. *MNRAS* 450:2327

Zuckerman B, Evans NJ. 1974. *Astrophys. J.* 192:149

Zwaan MA, Meyer MJ, Staveley-Smith L, Webster RL. 2005. *MNRAS* 359:30

Contents

Indexes

Errata

An online log of corrections to *Annual Review of Astronomy and Astrophysics* articles may
be found at http://www.annualreviews.org/errata/astro